Multiple thermotectonic events in a continuous metamorphic sequence, Mica Creek area, southeastern Canadian Cordillera

J.L. Crowley[1]*, E.D. Ghent[1], S.D. Carr[2], P.S. Simony[1], M.A. Hamilton[3]

[1]Department of Geology and Geophysics, University of Calgary, Calgary, AB T2N 1N4, Canada, [2]Department of Earth Sciences and Ottawa-Carleton Geoscience Centre, Carleton University, Ottawa, ON K1S 5B6, Canada, [3]Geological Survey of Canada, 601 Booth Street, Ottawa, ON K1A 0E8, Canada, *now at Department of Earth Sciences, Memorial University of Newfoundland, St. John's, NF A1B 3X5, Canada <jcrowley@sparky2.esd.mun.ca>
(Received January 10, 2000; Published May 24, 2000)

Abstract

U-(Th)-Pb isotope dilution and SHRIMP dating indicates that multiple periods of metamorphism and deformation occurred between ~160 and 60 Ma in the Mica Creek area, southeastern Canadian Cordillera. The metamorphic sequence (Barrovian assemblages in the garnet zone through the sillimanite–K-feldspar zone), fold generations, and Neoproterozoic stratigraphy are apparently continuous across the area, yet it broadly lies between regions that were tectonized at different times, Middle Jurassic to the east and middle Cretaceous - Paleocene to the west. Our dating along a north (lowest metamorphic grade) to south (highest grade) transect shows that three, km-scale tectonic age domains exist. In garnet schist of domain 1, peak metamorphism occurred at ~163 Ma and a minor thermal overprint occurred at 70-60 Ma. In migmatitic kyanite schist of domain 2, monazite inclusions in garnet grew at 110 Ma, matrix monazite and monazite inclusions in kyanite grew at ~85-73 Ma, and rims of some grains grew at ~60 Ma. Kyanite growth during peak metamorphism must have occurred after 73 Ma, possibly during intrusion of 61 Ma leucosome. In migmatitic kyanite schist and sillimanite schist of domain 3, peak metamorphism occurred at 99-93 Ma, and lesser thermal events occurred at ~280, 160, 110, and 70 Ma. We thus conclude that the thermal peak of metamorphism took place at different times in each domain, with peak events coinciding with secondary events in other domains. Age constraints on S_{1+2} are provided by dating variably deformed granitoid rocks. S_{1+2} developed before 72 Ma in domain 1, at least partly at 61-58 Ma and 122-63 Ma in domains 2 and 3, respectively. Our findings show that the Mica Creek area is the only known region in the southeastern Canadian Cordillera that was affected by the five recognized major periods of tectonism (175-160, 140-120, 110, 100-90, and 75-50 Ma). The key to understanding the geologic history is determining why several metamorphic and deformation events spanning 100 Myr occurred within a single tectonometamorphic complex with apparent geologic continuity. If continuity is only apparent, the domains may have been tectonically assembled along cryptic, unrecognized shear zones. However, if continuity does indeed exist, the events must have been locally superimposed on the complex.

Keywords: Canadian Cordillera, metamorphism, monazite, U-Th-Pb geochronology

Introduction

The Mica Creek area occupies an important position in the metamorphic core of southeastern Canadian Cordillera because it straddles the only part of the boundary between the Selkirk and Monashee mountains across which metamorphic, structural, and stratigraphic elements are mapped as continuous (Simony et al., 1980) (Fig. 1). The area lies on the northeast flank of a large northwest-trending belt of high-grade metamorphic rocks, which is cored by sillimanite and sillimanite + K-feldspar schists, and it includes the adjacent metamorphic low, which is cored by garnet schists (Simony et al., 1980) (Fig. 1). The metamorphic high is a 200 x 60 km area that overlaps the Selkirk, Monashee, and Cariboo mountains (Read et al., 1991), and thus we refer to the metamorphic high, the low, and a narrow high to the north as the Selkirk-Monashee-Cariboo (SMC) complex.

The geologic continuity in the Mica Creek area is apparently contradictory with isotopic dating that suggests metamorphism and deformation occurred at different times in the adjacent parts of the SMC complex (Fig. 1); rocks in the Selkirks were tectonized in the Jurassic and then exhumed to relatively high structural levels (Shaw, 1980; Archibald et al., 1983; Brown et al., 1992; Colpron et al., 1996) before heating of structurally deeper rocks in the Monashees in the middle Cretaceous and Late Cretaceous-Eocene (Sevigny et al., 1989, 1990; Scammell, 1993; Parrish, 1995; Gibson et al., 1999; Crowley and Parrish, 1999). Parrish (1995) considered this pattern of structurally downward younging tectonism to be consistent with the thermal evolution of rocks in the hinterland of a fold and thrust belt that were progressively buried as the belt propagated toward the foreland. Our dating in the Mica Creek area will help us to understand how the timing of metamorphism and deformation varies across structural levels in the SMC complex, within an apparently continuous geologic sequence. This knowledge should result in improved tectonic models.

Samples were collected across a Barrovian metamorphic sequence that is continuous from the garnet zone in the regional metamorphic low to the sillimanite-migmatite zone in the adjacent high (Fig. 2). U-Pb isotope dilution thermal ionization mass spectrometric (IDTIMS) dating and backscattered electron imaging were performed on 16 samples. *In situ* dating with a sensitive high-resolution ion microprobe (SHRIMP) was performed on monazite in two of these samples in order to better relate the U-Pb ages to the timing of peak metamorphism. The timing of deformation along the transect was constrained by U-Pb dating of variably deformed granitoid rocks. Based on our findings, we propose a new tectonic model for the Mica Creek area that emphasizes a complex and multi-episodic metamorphic and deformation history.

Geologic setting

The SMC complex lies in the southern Omineca Belt (Fig. 1), the metamorphic and plutonic hinterland to the Rocky Mountain Foreland Belt of the Canadian Cordillera that developed subsequent to collision between accreted terranes and North America (Monger et al., 1982). The complex lies structurally below the accreted terranes and above the autochthonous Paleoproterozoic basement (Monashee and Malton complexes). Major periods of metamorphism, deformation, and plutonism in the southern Omineca Belt occurred at 175-160, 100-90, and 75-60 Ma (see Parrish (1995) for a compilation of age data). The ages of tectonism are generally

younger with increasing structural depth, but the relationship between structural depth and age is locally more complex, such as in the northern Monashee Mountains (Digel et al., 1998; this study). Rocks in the northern Selkirks and southern Cariboos (Fig. 1) underwent Barrovian metamorphism, development of kilometre-scale folds, and syn-tectonic plutonism at 175-160 Ma (Shaw, 1980; Archibald et al., 1983; Gerasimoff, 1988; Brown et al., 1992; Colpron et al., 1996). These rocks were then exhumed to high structural levels and intruded by 100 Ma undeformed plutons (Archibald et al., 1983; Crowley and Brown, 1994). Rocks in the northern Monashee Mountains (Fig. 1) were metamorphosed and deformed at mid-crustal depths and then exhumed after those in the Selkirks. Rocks at intermediate structural levels of the northern Monashees underwent high-grade metamorphism and associated anatexis at 100-90 Ma (Sevigny et al., 1989, 1990; Scammell, 1993), whereas those at the deepest levels of the orogen (Monashee complex) did not undergo high-grade metamorphism and associated anatexis until 80-50 Ma (Parrish, 1995; Gibson et al., 1999; Crowley and Parrish, 1999). Other rocks in the northern Monashees underwent an older (~140 Ma) metamorphism and a ~60 Ma sillimanite overprint (Digel et al., 1998). Compressional deformation and metamorphism in the northern Monashees ceased shortly before or during orogenic extension in the Eocene, which was accommodated on a regional scale by brittle-ductile normal fault systems (Parrish et al., 1988; Carr, 1995 and references therein).

Geothermobarometric studies indicate peak conditions of 540-700^{o}C and 5.8-7.2 kbar in the Mica Creek area (Ghent et al., 1982, 1983 and references therein). Temperatures determined by fluid inclusion (Stout et al., 1986) and oxygen isotope studies (Ghent and Valley, 1998) agree reasonably well with these estimates. Three Barrovian metamorphic zones in the area (Fig. 2) are defined by mineral assemblages in pelitic schist and the presence or absence of leucosome (Simony et al., 1980). In the northeast, at the head of Franchère Creek, the garnet zone is dominated by biotite-muscovite-garnet schist. Fine-grained kyanite and staurolite are locally present, leucosome is absent, and granitoid rocks are only present in the southernmost part. Metamorphic grade slightly increases from the garnet zone to the northeast, where fine-grained kyanite and staurolite are common in coarser grained rocks that contain trondhjemitic leucosome. Metamorphic grade rises more dramatically to the southwest from the garnet zone to the kyanite-migmatite zone (typified by muscovite-biotite-garnet-kyanite schist with granitic leucosome). The boundary between the garnet zone and kyanite-migmatite zone is poorly defined in the study area because it projects across low-alumina schist and amphibolitic gneiss on Mount Nagle; it is only confidently known that rocks to the north contain a minor amount of fine-grained kyanite and staurolite, whereas to the south, coarse kyanite is present, leucosome is abundant, and staurolite is generally absent. Along strike to the northwest, a discrete kyanite-staurolite zone lies between the garnet zone and kyanite-migmatite zone. The kyanite-sillimanite isograd is well-defined from the northern Selkirk Mountains to the eastern part of the northern Monashees (Fig. 1). The sillimanite-migmatite zone, which is southwest of the isograd, is typified by migmatitic muscovite-biotite-garnet-sillimanite schist. Staurolite is locally present. The muscovite-out isograd is a few kilometres south of the study area. One of our objectives is to use U-(Th)-Pb ages obtained along a transect from the garnet zone to sillimanite-migmatite zone to test whether this apparently continuous metamorphic sequence (Simony et al., 1980) is the same age throughout.

Three generations of folds were recognized by Simony et al. (1980). A macroscopic recumbent anticlinal (F_1) fold in the northern Monashee Mountains was mapped based on the presence of two identical, opposite-facing stratigraphic packages in the Neoproterozoic Windermere Supergroup (Simony et al., 1980; Pell and Simony, 1987). This fold, the Scrip nappe (Raeside and Simony, 1983), is southwest-verging and has an overturned limb that is >50 km long. Its axial surface trace lies in the lower pelite unit in the study area (Figs. 2, 3). The nappe was refolded by northeast-verging tight (F_2) folds that were overprinted by northeast-verging open to close (F_3) folds. The Mica Creek antiform is a large F_3 fold culmination centred on Mount Nagle (Fig. 3). The thermal peak of metamorphism was interpreted as having occurred during late stages of F_2 folding based on the relationships between index minerals and the structures. Folds of all three generations are approximately coaxial; they plunge gently to the northwest or southeast. The dominant penetrative foliation in the area is a composite of the F_1 and F_2 axial surfaces, termed S_{1+2}. We refer to the dominant foliation in a given outcrop as S_{1+2}, despite the knowledge that it may differ in age from S_{1+2} in other localities. One of our objectives is to use U-Pb ages obtained from variably deformed granitoid rocks to test whether S_{1+2} is the same age throughout, as is suggested by the similarity in the style and orientation of structures across the area.

A high-angle, northeast-trending brittle fault that is west of Mica Dam has a south-side-down offset of 1.5 km (Simony et al., 1980) (Fig. 2). This offset combined with the gentle southeast plunge of the Mica Creek antiform requires that higher structural levels lie southeast of the fault. The fault, which is presumably related to brittle normal faults in the Southern Rocky Mountain Trench to the east of the study area (Fig. 1), terminates at Nagle Creek (Fig. 2).

U-(Th)-Pb geochronology

We obtained zircon, monazite, and xenotime U-(Th)-Pb isotopic data from 16 samples. The data are presented in Tables 1 and 2, on a map (Fig. 2), and in concordia diagrams (Figs. 4-6). Results are summarized in a timeline (Fig. 14). For simplicity, the study area is divided into three domains according to monazite ages from the schists (Fig. 2). Domain 1 contains garnet zone schists in the northern part of the area that yield mainly ~160 Ma ages. Semipelitic schists that straddle the poorly defined migmatite-in and staurolite-out isograds are included in domain 1. Centrally-located domain 2 contains kyanite-migmatite zone schists that yield mainly 80-60 Ma ages. Domain 3 in the southern part contains kyanite-migmatite and sillimanite-migmatite zone schists that yield mainly 99-93 Ma ages.

Analytical methods

U-Pb IDTIMS geochronology followed procedures outlined by Parrish et al. (1987); microcapsules were used for mineral dissolution (Parrish, 1987), a mixed ^{233}U-^{235}U-^{205}Pb tracer was added to the samples (Parrish and Krogh, 1987), isotopic analyses were carried out on a multicollector mass spectrometer (Roddick et al., 1987), and estimation of errors was done using numerical error propagation (Roddick, 1987). Decay constants used are those recommended by Steiger and J ger (1977). Discordia lines through analyses were calculated with the use of a modified York (1969) regression (Parrish et al., 1987), which takes scatter into account. Mineral selection and the U-Pb chemistry were performed in the geochronology laboratory at Carleton

University, where U and Pb blanks were less than 5 pg. Isotopic ratios were determined on a MAT 261 mass spectrometer at Carleton University. The fractions analyzed comprised single grains or single fragments of grains. The clearest and least magnetic zircons with the fewest inclusions and cracks were analyzed. All zircons had an igneous morphology (i.e., prismatic and elongate) and were abraded (Krogh, 1982). The clearest xenotimes and monazites with the fewest inclusions were also analyzed. Grains that contain xenocrystic cores visible with a microscope in transmitted light were avoided.

Ion microprobe analysis of monazite in polished thin sections was performed using the SHRIMP II at the Geological Survey of Canada, following procedures outlined by Stern (1997) and Stern and Sanborn (1998). Instrumental bias in the measured Pb/U and Pb/Th ratios was corrected for by an empirically-derived calibration of the linear relationships between $^{206}Pb^{+}/UO^{+}$ vs. UO_2^{+}/UO^{+} and $^{208}Pb^{+}/ThO^{+}$ vs. UO_2^{+}/UO^{+}, determined on sets of three natural monazite standards (GSC samples 2908, 3345 and 4170), grains of which were set in epoxy into roughly 2 mm diameter pits drilled into each thin section. Following repolishing, the sections were coated by evaporation under vacuum with approximately 12 nm of conductive high purity Au (Aesar 99.9999%) and then imaged with a Cambridge Instruments scanning electron microscope equipped with a backscattered electron (BSE) detector. Targeted areas of exposed monazites were sputtered using a mass-filtered O_2^{-} primary beam operating in Kohler illumination mode to effect even sputtering. Analysis of monazite in sample 1 was made using a primary beam diameter of roughly 20 x 26 μm, whereas grain size limitations and smaller zonal domain boundaries (as identified in BSE) in sample 9 required a spot size of roughly 8 x 10 μm. Primary ion beam currents were typically 1.0-1.3 nA and 0.6 nA for the larger and smaller spot sizes, respectively. The operational mass resolution (1% peak height) over the course of the analyses was 5550. Isotopic ratios were corrected for common lead using ^{204}Pb. Determination of U abundances in the unknowns was calculated through the linear relationship between measured $^{203}CePO_2^{+}/UO^{+}$ and U concentration; uncertainties in the U content and in the derived Th abundance are estimated at ± 20% (Stern and Sanborn, 1998). Uncertainties for isotopic ratios and ages shown in Table 2 are 1σ, whereas the error ellipses in Figure 5 are 2σ.

Guidelines for age interpretations

Monazite and xenotime U-Pb IDTIMS ages in most samples vary over a few million years or more and many are reversely and normally discordant (Figs. 4-6). Proper interpretation of the age spread within a sample and the discordance is crucial to interpreting whether the dates represent primary or secondary growth ages, recrystallization ages, cooling ages, or mixed ages.

The reverse discordance (i.e., $^{206}Pb/^{238}U$ ages > $^{207}Pb/^{235}U$ ages) that is exhibited by some monazite analyses is attributed to unsupported ^{206}Pb that resulted from incorporation of excess ^{230}Th upon crystallization (Schärer, 1984; Parrish, 1990). Thus, only $^{207}Pb/^{235}U$ ages are reported here for reversely discordant analyses. Corrections for excess ^{206}Pb to the $^{206}Pb/^{238}U$ ages from granitoid rocks were not made using the method outlined by Schärer (1984) because Th/U whole rock ratios were not measured. However, applying the correction with typical Th/U whole rock ratios from similar types of granitoid rocks (Schärer, 1984; Parrish, 1990) yields concordant U-Pb ages. As pointed out by Parrish (1990), there is little justification for the use of this correction on metamorphic monazite because it is difficult to determine the Th/U ratios of the fluids in

which the mineral grew. Corrections for a deficit in ^{230}Th upon crystallization in zircon and xenotime (Schärer, 1984; Parrish, 1990) result in a maximum of 0.1 Ma increase in the ^{206}Pb/^{238}U ages.

Reversely discordant analyses are interpreted as approximating primary growth ages because grains with inheritance or ones that suffered substantial diffusive Pb loss, overgrowth, or recrystallization yield concordant or normally discordant dates. Diffusive Pb loss is ruled out in all analyses because many studies have shown that monazite is highly resistant to this thermally induced process (Crowley and Ghent, 1999 and references therein). However, we cannot rule out that the grains with reverse discordance underwent a minor amount of overgrowth or recrystallization, which commonly occur in monazite (Crowley and Ghent, 1999 and references therein). Concordant U-Pb dates are interpreted as reflecting primary growth ages for some analyses and as mixed ages for other analyses. The latter analyses are thought to be composed of primary domains with reverse discordance due to excess ^{206}Pb (Schärer, 1984; Parrish, 1990) and secondary domains. Normally discordant U-Pb dates are interpreted as reflecting mixed ages. For the cases in which three or more analyses define linear arrays (discordias), upper intercepts of the discordias are interpreted as ages of primary growth and lower intercepts are interpreted as ages of secondary growth. Reverse discordance in the primary growth domain may result in an upper intercept that underestimates the age of primary growth, whereas reverse discordance in the secondary domain may result in a lower intercept that overestimates the age of secondary growth. Discordias that are regressed through only two analyses are considered to be meaningful if the upper and lower intercepts have geological significance in nearby rocks.

Monazites from the granitoid rocks could have igneous and (or) metamorphic and (or) xenocrystic origins, and proper interpretation of crystallization history is crucial for attributing age significance to the U-Pb dates. The interpretations made in the following section are based on zircon data from the rock (if available), grain morphology, U-Pb data from nearby rocks, and geologic setting. In general, euhedral monazites are interpreted as igneous, whereas xenoblastic grains with numerous embayments are interpreted as metamorphic.

Isotopic data and age interpretations

Pelitic schists considered in this study contain garnet, aluminosilicates, biotite, muscovite, plagioclase, quartz, and accessory minerals (monazite, zircon, etc.). Semipelitic schists generally lack garnet and aluminosilicates. Pegmatite, leucogranite, and leucosome samples contain biotite, plagioclase, K-feldspar, quartz, and accessory minerals (monazite, zircon, etc.), and some samples also contain tourmaline, muscovite, and garnet. Polished grains and thin sections were imaged with BSE microscopy. Varying degrees of brightness in the images correspond to variations in the average atomic number, which, in monazite and xenotime, are mainly controlled by Th and U concentrations.

Domain 1. Sample 9 is from garnet-biotite-muscovite schist at the head of Franchère Creek (Fig. 2). S_{1+2}, which is defined by aligned biotite and muscovite, wraps around garnet. Quartz-filled pressure shadows lie adjacent to garnet, which contains an internal fabric that differs in orientation from S_{1+2} (Figs. 7, 8b). These relationships require that S_{1+2} developed, at least in part, after garnet growth. Monazites are xenoblastic, elongate, and embayed. BSE imaging of

thin sections suggests that monazites lie within S_{1+2}, contain numerous quartz inclusions, and have highly irregular grain boundaries (Figs. 8a-c, 9a, b); these features impart a ragged appearance to the grains. Xenotime and zircon are abundant in the matrix and exist as inclusions in garnet. Only one monazite inclusion in garnet was found.

Four monazite IDTIMS analyses on picked separates define a discordia with upper and lower intercepts of 162 +5 / -4 and 63 ± 14 Ma, respectively (mean square of weighted deviates (MSWD) = 0.9) (Table 1, Fig. 5a). Discordance is 1-41% (as measured along the discordia from the upper intercept). The high spatial resolution of the SHRIMP was used to analyze *in situ* matrix monazite that lies within S_{1+2}, and a monazite inclusion in garnet (Table 2, Fig. 5a). The locations of the grains in thin section are shown in Fig. 7 and the locations of the SHRIMP spots (size of 8 x 10 μm) in two matrix grains are shown in Fig. 9a, b. Seventeen analyses from seven matrix grains yield $^{208}Pb/^{232}Th$ ages that fall into two age groups that are spatially related to position in the grains. Nine spots in grain interiors yield ages of ~173-144 Ma. The $^{206}Pb/^{238}U$ ages are both younger and older than the $^{208}Pb/^{232}Th$ ages, typically by 1-6 Myr, and they have a narrower age range of ~159-149 Ma. Eight spots in grain rims yield $^{208}Pb/^{232}Th$ ages of ~62-56 Ma. The $^{206}Pb/^{238}U$ ages are both younger and older by a few million years. U and Th concentrations are similar in all analyses and BSE imaging did not detect a difference in Th concentration between cores and rims. A single spot analysis of a monazite inclusion in garnet is reversely discordant, yielding a $^{208}Pb/^{232}Th$ date of ~161 Ma and a $^{206}Pb/^{238}U$ date of ~183 Ma.

Grains that were dated by the IDTIMS method are interpreted as mixtures of monazite that grew at 162 +5 / -4 and 63 ± 14 Ma, the upper and lower intercepts of the discordia defined by the analyses, respectively (Fig. 5a). The 1-41% discordance indicates that some grains were composed of a minor amount of ~63 Ma monazite, whereas others were composed of a substantial amount. The SHRIMP dating confirms that cores and rims grew at ~160 and ~60 Ma, respectively (Figs. 9a, b). SHRIMP ages between 160 and 140 Ma probably represent spots that overlapped two age domains rather than growth during that interval. The same may be true for ages between 63 and 60 Ma. The $^{208}Pb/^{232}Th$ date from a monazite inclusion in garnet is the same as the ages from the cores of matrix monazites, yet it is uncertain whether this date represents a growth age because the $^{206}Pb/^{238}U$ date is considerably older at ~183 Ma.

Sample 16 is from biotite-muscovite schist at the head of the north branch of Encampment Creek (Fig. 2). Xenotime and monazite are xenoblastic, typically subrounded, and embayed. BSE imaging of xenotimes suggests complex U zoning (Figs. 10a, b), as the numerous zoning truncations indicate multiple episodes of dissolution, recrystallization, and overgrowth. Xenotime and monazite are included in quartz and feldspar and also lie along biotite and muscovite grain boundaries (Fig. 8a). Three xenotime analyses and one monazite analysis define a discordia with upper and lower intercepts of 163 +5 / -3 and 81 +18 / -20 Ma, respectively (MSWD = 0.2) (Table 1, Fig. 4a). Discordance is 9-23% (as measured along the discordia from the upper intercept). The upper intercept of ~163 Ma is interpreted as the age of primary xenotime and monazite growth. The lower intercept of 81 +18 / -20 Ma is interpreted as the age of secondary growth or recrystallization.

Sample 18 is from a 1-3 m thick biotite pegmatite layer at the head of the north branch of Encampment Creek (Fig. 2). This is the northernmost granitoid found in the study area. It is

concordant with S_{1+2} in the host semipelitic schist (sample 16) and contains a strong layer-parallel foliation defined by flattened quartz and feldspar (Fig. 12a). Most of the ductile deformation responsible for S_{1+2} is interpreted as occurring after pegmatite crystallization. Monazites are xenoblastic, typically subrounded, and embayed. BSE imaging of monazites suggests negligible Th zoning. Zircons are doubly terminated and subequant. BSE imaging of zircons suggests that cores with complex, patchy zoning are overgrown by oscillatory zoned rims (Figs. 10f, g).

Three monazite analyses define a discordia with upper and lower intercepts of 146 ± 11 and 69 +5 / -6 Ma (MSWD = 0.0) (Fig. 6a). Discordance is 28, 77, and 95% (as measured along the discordia from the upper intercept). The youngest analysis overlaps concordia with a $^{207}Pb/^{235}U$ date of 73 Ma. Four zircon analyses are discordant (Fig. 6b), two of which plot relatively close to concordia at 160 Ma. There are two possible interpretations of these data: (i) the ~69 Ma lower intercept defined by the monazite discordia represents the igneous crystallization age and the 146 ± 11 Ma upper intercept represents the age of inherited monazite, and (ii) ~69 Ma is the age of secondary monazite and 146 ± 11 Ma approximates the crystallization age, with the actual age perhaps being slightly older if the primary monazites were reversely discordant. We prefer the second interpretation for three reasons. First, a pegmatite layer located 6 km to the south with similar composition and structural setting (sample 19) is thought to have crystallized at 171 ± 12 Ma and was intruded by a 72.0 ± 0.5 Ma undeformed pegmatite dyke (sample 20). Second, although the zircons contain significant inheritance of variable age, regression of discordias through the uppermost and lowermost pairs of analyses yields identical lower intercepts of 158 Ma, which are thought to reflect the age of igneous zircon crystallization. The 146 ± 11 Ma upper intercept defined by monazite is slightly younger than 158 Ma, which is the expected result if the monazites are indeed mixtures of primary domains that were slightly reversely discordant at 158 Ma (reverse discordance is common in primary monazites from Cordilleran granitoids) and Cretaceous secondary domains. Third, the monazite morphology (xenoblastic, subrounded, embayed) is similar to metamorphic monazite in adjacent schists.

Sample 19 is from a 0.5 m thick garnet-muscovite-biotite pegmatite layer at the head of a south branch of Encampment Creek, northeast of Mount Nagle (Fig. 2). The layer has the same appearance and structural setting as sample 18; it is concordant with S_{1+2} in the host psammite and contains a strong layer-parallel foliation (Fig. 12b). Most of the ductile deformation responsible for S_{1+2} is interpreted as occurring after crystallization. Zircons are elongate (aspect ratio of 3:1) and contain dark zones and cracks that suggest extensive radiation damage. BSE imaging suggests core and rim relationships similar to those in sample 18 (Figs. 10h, i). Four zircon analyses define a discordia with upper and lower intercepts of 1053 ± 2 and 171 ± 12 Ma (MSWD = 2.0) (Fig. 6c). Discordance is 5-20% (as measured along the discordia from the upper intercept). Another zircon analysis lies above this discordia. Forcing a discordia with a lower intercept of 170 Ma through this analysis yields an upper intercept of 1032 ± 2 Ma. Discordance is 3%. The 1053 ± 2 Ma upper intercept is interpreted as an age of inheritance in sample 19 rather than a crystallization age because the host metasedimentary rocks are correlated with the Neoproterozoic Windermere Supergroup. The 171 ± 12 Ma lower intercept is interpreted as the igneous crystallization age.

Sample 20 is from a 0.3-0.5 m thick garnet-muscovite-biotite pegmatite dyke at the head of a south branch of Encampment Creek (Fig. 2). The vertical north-striking dyke is highly discordant to the vertical west-striking S_{1+2} in the host psammite (Fig. 12c). It lacks planar and linear deformation fabrics at the handspecimen scale. The structural setting indicates that S_{1+2} developed before pegmatite intrusion. Monazites are clear and blocky. BSE imaging suggests uniform Th concentrations throughout. Three significantly reversely discordant monazite IDTIMS analyses have $^{207}Pb/^{235}U$ ages of 72.2-71.8 Ma (Table 1, Fig. 6d). The interpreted igneous crystallization age is 72.0 ± 0.5 Ma.

Sample 22 is from biotite-muscovite schist at the head of a south branch of Encampment Creek, northeast of Mount Nagle (Fig. 2). Monazites are xenoblastic, typically subrounded, and embayed. BSE imaging shows an irregular distribution of Th-rich zones in some grains (Figs. 10c, d) in a manner that suggests formation during secondary mineral growth. Monazite is commonly intergrown with xenotime and zircon. Elongate grains lie within S_{1+2} at muscovite and biotite grain boundaries (Fig. 8b), whereas other grains are associated with pyrite. Four monazite analyses define a discordia with upper and lower intercepts of 163 ± 3 and 88 ± 2 Ma, respectively (MSWD = 0.3) (Table 1, Fig. 4b). The two analyses that plot closest to the upper intercept are 5 and 18% discordant. The two youngest analyses are concordant within uncertainty with $^{207}Pb/^{235}U$ ages of 91 and 89 Ma. The upper intercept of ~163 Ma is interpreted as the age of primary monazite growth. Although it cannot be ruled out that the two 90 Ma analyses are mixtures of domains that grew before and after 90 Ma, with either component being reversely discordant, a mixture is considered to be unlikely given that the two analyses yield almost identical ages; it would be fortuitous for two mixed grains to have the same portions of primary and secondary domains. Thus, a period of secondary growth at 90 Ma is likely.

Domain 2. Sample 1 is from migmatitic muscovite-garnet-kyanite-biotite schist in a roadcut on Highway 23, 0.5 km south of Mica Dam (Fig. 2). S_{1+2}, which is defined by aligned kyanite, biotite, and muscovite, wraps around garnet. Garnet contains an internal foliation that is discordant to S_{1+2}, requiring that S_{1+2} developed, at least in part, after garnet growth. Monazites are xenoblastic, typically subrounded, and embayed. BSE imaging suggests uniform Th concentrations throughout. Grains are abundant in the matrix and as inclusions in kyanite, and they rarely exist as inclusions in garnet.

A monazite IDTIMS analysis is concordant at 74 Ma (Table 1, Fig. 5b). Two other analyses are reversely discordant with $^{207}Pb/^{235}U$ ages of 71 and 70 Ma. These three analyses define a discordia with upper and lower intercepts of 253 +198 / -162 and 73 +2 / -28 Ma, respectively (MSWD = 0.0). The normally discordant analyses are ~99% discordant (as measured along the discordia from the upper intercept). The SHRIMP was used to date monazite inclusions in kyanite and garnet, and monazites that lie in the matrix within S_{1+2} (Table 2, Fig. 5b). The inclusions are interpreted as growing prior to growth of the host mineral because there are no visible cracks in the host along which the inclusions could have formed. The locations of the grains in thin section are shown in Fig. 11 and the locations of the SHRIMP spots (size of 20 x 26 μm) in one of these grains are shown in Fig. 9c. The $^{208}Pb/^{232}Th$ ages are generally concordant with the $^{206}Pb/^{238}U$ ages. Three spots in a monazite inclusion in a garnet rim yield $^{208}Pb/^{232}Th$ ages of ~113-109 Ma. This monazite has a lower U concentration relative to the other analyzed monazites in the sample. Nine spots in five monazite inclusions in kyanite yield

$^{208}Pb/^{232}Th$ ages of ~83-73 Ma. Seven spots in three matrix grains yield comparably indistinguishable ages of ~84-74 Ma, and two spots in the rim of a matrix grain yield younger ages of ~64 and 61 Ma (Fig. 9c). U and Th concentrations are similar in these analyses. BSE imaging shows that a band of slightly higher Th concentration (not analyzed) separates the core spots from the rim spots.

The rather narrow age spread in the three SHRIMP ages of ~110 Ma from the monazite inclusion in a garnet rim suggests that some monazite grew then. The two normally discordant IDTIMS analysis indicate that pre-74 Ma monazite exists in sample 1; an imprecise Phanerozoic age is interpreted from the upper intercept of the discordia. The SHRIMP ages may be used to interpret whether the IDTIMS analyses are mixtures of monazite domains that are older and younger than the IDTIMS $^{207}Pb/^{235}U$ ages of 74-70 Ma. Given that the SHRIMP spots in matrix monazite cores yield ages of 86-72 Ma and rims yield 66-60 Ma ages (Table 2, Fig. 9c), it is possible that the IDTIMS analyses were composed of domains that are as old as 86 Ma and as young as 60 Ma. Despite the small size of the SHRIMP spots, it is also possible that the SHRIMP ages from matrix grains are mixed ages (i.e., the spots overlapped multiple age domains), even though in most cases, discrete domains were not visible in the BSE images. Taking grain M-1 as an example (Fig. 9c), it is probable that the matrix core grew at ~83 Ma, the rim grew at ~60 Ma, and the two spots that lie between these domains (with ages of 78 and 74 Ma) overlapped the two domains. It will only be possible to determine precisely when various parts of the grains grew upon dating with a smaller spot size. Pending this work, we suggest that the older parts of the matrix grains grew at ~85-75 Ma and the younger parts grew at ~60 Ma. Given that ~60 Ma ages were not obtained from five dated monazite inclusions in kyanite, it is possible that ~60 Ma rims do not exist and thus the 85-72 Ma ages closely represent growth ages. Again, dating at a higher spatial resolution is needed before confident interpretations can be made.

Sample 2 is from a pegmatitic muscovite leucosome lens (maximum thickness of 0.3 m) in a roadcut on Highway 23, 0.5 km south of Mica Dam (Fig. 2). The lens is concordant with S_{1+2} in the host migmatitic kyanite schist (sample 1) (Fig. 12d). It is a boudin in a train of leucosome boudins that is thought to have formed by shearing of an anatectic melt. It lacks planar and linear deformation fabrics at the handspecimen scale. Lenses with similar structural relationships are ubiquitous in the roadcut, and some of them contain kyanite. The structural setting is interpreted as indicating that some S_{1+2} development occurred after leucosome crystallization, yet it is possible that most development occurred before then (i.e., there was only reactivation of S_{1+2} after crystallization). Monazites are clear and euhedral. Zircons are elongate (aspect ratio of 3:1) and contain dark zones and cracks that suggest extensive radiation damage. Two reversely discordant monazite IDTIMS analyses have $^{207}Pb/^{235}U$ ages of 61-60 Ma (Table 1, Fig. 6e). One zircon IDTIMS analysis is concordant at 61 Ma and another analysis is slightly discordant. The interpreted igneous crystallization age is 60.7 ± 0.5 Ma.

Sample 3 is from migmatitic garnet-biotite-kyanite schist in a roadcut at Potlatch Creek (Fig. 2). Monazite grains have a range of morphologies, including angular xenoblastic, rounded xenoblastic, and idioblastic. BSE imaging suggests an irregular distribution of moderately Th-rich zones in many grains (Fig. 10e). Elongate grains lie within S_{1+2} at biotite, quartz, and kyanite grain boundaries (Fig. 8c). Three monazite analyses lie on or near concordia with

$^{207}Pb/^{235}U$ ages of 132-124 Ma (Fig. 4c). A fourth analysis is normally discordant with a $^{207}Pb/^{235}U$ date of 126 Ma. The grains are interpreted as mixtures of domains that grew before and after 132 and 124 Ma, respectively. We make this interpretation two reasons. First, the presence of a normally discordant analysis requires that pre-132 Ma primary monazite domains exist in sample 3. Forcing a discordia through this analysis from a lower intercept of 80-70 Ma, the dominant age of monazite growth in nearby sample 1, yields an upper intercept that agrees closely with the 163 Ma age of primary monazite growth in domain 1. Thus, it is likely that the grain grew at ~163 Ma and underwent secondary growth or recrystallization at 80-70 Ma, similar to grains in domain 1. Second, the three analyses that lie on or near concordia define a discordia with a lower intercept of 69 Ma. The upper intercept of this discordia plots 0.7 Myr above 163 Ma, the age of primary growth in domain 1. Thus, we suggest that these analyses are composed of ~163 Ma primary monazite that is reversely discordant by 0.7 Myr due to excess ^{206}Pb (Schärer, 1984; Parrish, 1990) and secondary monazite that grew at 80-70 Ma. In this interpretation, secondary monazite contains 30-40% of the Pb in the grains.

Sample 4 is from a 2 m thick muscovite pegmatite dyke at the top of the Mica Dam spillway (Fig. 2). The vertical dyke is highly discordant to gently dipping S_{1+2} in the host migmatitic kyanite schist (Fig. 12e). It lacks planar and linear deformation fabrics at the handspecimen scale. The structural setting indicates that S_{1+2} developed before pegmatite intrusion. Monazites are cloudy and euhedral. BSE imaging suggests uniform Th concentrations throughout. Three reversely discordant monazite IDTIMS analyses have $^{207}Pb/^{235}U$ ages of 59.8-58.0 Ma (Table 1, Fig. 6e). The interpreted igneous crystallization age is 58.4 ± 0.5 Ma.

Sample 24 is from a biotite-muscovite pegmatite layer up to 2.5 km thick on the shore of Kinbasket Lake, 0.8 km west of Potlatch Creek (Fig. 2). In spring, when the water level in the lake drops >20 m, the layer is exposed in continuous outcrop along a strike length of 32 m. The layer is beaded (i.e., exhibits a pinch-and-swell structure) and largely parallels S_{1+2} and lithologic layering (tightly folded and transposed bedding) in the host schist. S_{1+2} envelopes the thicker beads, yet locally the pegmatite contacts cut across S_{1+2} and lithologic layering. Foliation-parallel screens exist in the thicker beads. The foliation in the layer is due to aligned coarse mica, which is probably inherited, and scattered flattened quartz and feldspar grains. The necks are not more foliated than the beads, and convolutions in the contacts are not sheared. These observations indicate that the beaded structure is not simply the result of boudinage of the layer, but it formed, at least in part, during pegmatite emplacement. The structural setting is interpreted as indicating that some S_{1+2} development occurred during or after pegmatite crystallization, yet it is possible that most development occurred before then (i.e., there was only reactivation of S_{1+2} after crystallization). The characteristics of sample 24 contrast with those of the highly foliated and folded pegmatite layers in the same outcrop and in domain 1 (samples 18 and 19).

Monazites are clear and euhedral. BSE imaging suggests uniform Th concentrations throughout most grains, but one grain has slight compositional variability that suggests it underwent significant dissolution and multiple periods of growth. Seven reversely discordant monazite analyses have $^{207}Pb/^{235}U$ ages that fall into three groups: 69.1-68.1 (n = 2), 65.0-64.4 (n = 1), and 63.8-63.1 Ma (n = 4) (Fig. 6f). The interpreted igneous crystallization age is 63.5 ± 0.5 Ma based on the youngest four analyses. Monazites in oldest group are thought to be xenocrystic grains that were inherited from the host schist because they are coeval with metamorphic

monazite from nearby sample 1. The analysis with an intermediate age is thought to be a mixture of igneous and inherited monazite.

Domain 3. Sample 6 is from a 0.2-2 m thick muscovite-biotite leucogranite layer in a roadcut on Highway 23 south of Mica Creek Village (Fig. 2). The layer is concordant with S_{1+2} in the host migmatitic kyanite schist (sample 26) (Fig. 12g) and contains a weak layer-parallel foliation defined by biotite and flattened quartz and feldspar. The layer has been pulled apart into boudins. Monazites are xenoblastic, typically subrounded, and embayed. Zircons are elongate (aspect ratios of 3:1 to 6:1). Four reversely discordant monazite analyses have $^{207}Pb/^{235}U$ ages of 98-95 Ma (Fig. 6g). One analysis is concordant at 96 Ma. A xenotime analysis lies just below concordia at 92 Ma. Two concordant zircon analyses have $^{207}Pb/^{235}U$ ages of 122 Ma (Fig. 6h). Another analysis lies just below concordia with a $^{207}Pb/^{235}U$ date of 123 Ma. Based on the igneous morphology of the zircons, the two concordant zircon analyses are interpreted as reflecting igneous crystallization at 122.0 ± 1.0 Ma. The ages of 98-95 and 92 Ma are interpreted as metamorphic monazite and xenotime growth ages, respectively, for three reasons. First, the dates are considerably younger than the igneous crystallization age of the rock that is interpreted from zircons with igneous morphology. Second, the dates are coeval with metamorphic monazite growth ages in the host schist (sample 26). Third, the morphology of the monazite (xenoblastic, subrounded, embayed) is similar to metamorphic monazite in adjacent schists.

Sample 7 is from a 2 m thick muscovite pegmatite dyke in a roadcut on Highway 23 south of Mica Creek Village (Fig. 2). The vertical dyke is highly discordant to gently dipping S_{1+2} in the host migmatitic kyanite schist (sample 26) and leucogranite layers (sample 6). It lacks planar and linear deformation fabrics at the handspecimen scale. The structural setting indicates that S_{1+2} developed before pegmatite intrusion. Monazites are clear and euhedral. Four reversely discordant monazite analyses have $^{207}Pb/^{235}U$ ages of 63.1-62.3 Ma (Fig. 6f). The interpreted igneous crystallization age is 62.7 ± 0.5 Ma.

Sample 26 is from migmatitic garnet-biotite-muscovite-kyanite schist in a roadcut on Highway 23 south of Mica Creek Village (Fig. 2). Most monazites are xenoblastic, subrounded, and embayed. Other grains are subidioblastic. BSE imaging suggests domains with slightly variable Th concentrations, with the highly embayed boundary between domains suggesting significant dissolution and multiple periods of growth. Large elongate grains lie within S_{1+2}, mostly as inclusions in biotite (Fig. 8d) and along biotite, quartz, and kyanite grain boundaries. Some grains exist as inclusions in kyanite and garnet. Given the complex zoning, it is not surprising there is a diverse pattern of U-Pb ages (Fig. 4d). Three reversely discordant monazite analyses have $^{207}Pb/^{235}U$ ages of 96-93 Ma. A concordant analysis, a slightly normally discordant analysis, and a slightly reversely discordant analysis have $^{207}Pb/^{235}U$ ages of 94, 98, and 112 Ma, respectively. Two other highly discordant analysis and the concordant analysis define a discordia with an upper intercept of 276 ± 19 Ma (MSWD = 0.1). Discordance is 91 and 97% (as measured along the discordia from the upper intercept). The four 98-93 Ma analyses are interpreted as reflecting the age of dominant monazite growth. Monazite that grew at ~276 Ma must exist in the highly discordant analyses. Although it cannot be ruled out that the slightly reversely discordant analysis with a age of 112 Ma is a mixture of 94 Ma monazite and reversely discordant older monazite, 112 Ma is thought to reflect monazite growth given that two coeval

monazites were dated in a nearby schist (sample 28) and a coeval monazite inclusion in garnet was dated in domain 2 (sample 1).

Sample 28 is from migmatitic garnet-biotite-muscovite-kyanite schist in a roadcut in Soards Creek valley (Fig. 2). Monazites are xenoblastic, typically subrounded, and embayed. BSE imaging suggests domains with slightly variable Th concentrations. Some grains show core-rim relationships, and the embayed boundary between the domains suggests that the core underwent significant dissolution before formation of the rim. Other grains are composed of numerous, relatively low-Th, elliptical domains that are enclosed by Th-richer monazite. Large elongate grains lie within S_{1+2}, mostly as inclusions in biotite and muscovite and at biotite, muscovite, and kyanite grain boundaries (Fig. 8e). Given the complex zoning, it is not surprising that there is a diverse pattern of U-Pb ages (Fig. 4e). Three reversely discordant monazite analyses have $^{207}Pb/^{235}U$ ages of 111, 96, 68 Ma. One analysis is concordant at 109 Ma. Two normally discordant analyses lie along a discordia with upper and lower intercepts of 155 ± 11 and 75 ± 6 Ma. Discordance is 45 and 84% (as measured along the discordia from the upper intercept). Reverse discordance is interpreted as reflecting monazite growth at 110, 96, and 68 Ma. The age of primary monazite in the normally discordant analyses is interpreted as 155 ± 11 Ma from the upper intercept of the discordia, and the age of secondary monazite is interpreted as 75 ± 6 Ma from the lower intercept. It is noteworthy that four periods of monazite growth (~160, 110, 96, and 70 Ma) are deduced from six dated grains.

Sample 29 is from migmatitic garnet-staurolite-sillimanite-biotite-muscovite schist in a roadcut in Soards Creek valley (Fig. 2). Monazites are xenoblastic and embayed. BSE imaging suggests domains with slightly variable Th concentrations, some of which are patchy and blocky and others are thin and laminar. The largest grains are associated with ilmenite and pyrite. Elongate grains lie within S_{1+2} as inclusions in biotite, whereas others are included in garnet and staurolite (Fig. 8f). Four monazite analyses are concordant or slightly reversely discordant with $^{207}Pb/^{235}U$ ages of 101, 98, 96, and 94 Ma (Fig. 4f). Another analysis is normally discordant, and forcing a discordia with a lower intercept of 95 Ma through it yields an upper intercept of 157 ± 14 Ma. Discordance is 59% (as measured along the discordia from the upper intercept). The four analyses with 100-94 Ma ages are interpreted as reflecting the time of dominant monazite growth. The discordant analysis probably contains primary monazite that grew at 157 ± 14 Ma.

Garnet zoning

Analytical methods

Garnet compositions were determined by analyzing carbon-coated, polished thin sections on the ARL-SEMQ electron microprobe at the University of Calgary. The accelerating voltage was 15 kV, the beam current was 150 nA, and a focused beam diameter of ~1 μm was used. Natural minerals and oxides were used as standards for the nine element analyses. Data reduction was performed according to the procedures of Bence and Albee (1968) and Nicholls and Stout (1986).

Zoning profiles

Garnets in four nonmigmatitic schists from domain 1 were analyzed (Fig. 2). Garnets in garnet schists are strongly zoned in Fe, Mg, Ca, and Mn (Fig. 13a, b). For example, the spessartine mole fraction varies from 0.09 (core) to 0.02 (rim) in sample 9 and from 0.24 (core) to 0.05 (rim) in sample 13. Zoning in a staurolite-garnet schist (sample 11) is similar. In contrast, garnet zoning in a kyanite-staurolite schist (sample 14) is weak; spessartine varies from 0.01-0.02. Garnets in two migmatitic kyanite schists from domain 2 were analyzed (Fig. 2). They are weakly zoned in Fe, Mg, Ca, and Mn (Fig. 13c, d); the spessartine mole fraction is 0.02-0.03 in sample 1 and 0.06-0.08 in sample 3.

Interpretation of zoning

Strongly zoned profiles in samples 9, 11, and 13 (domain 1) indicate that garnet formed during a single stage of growth and diffusional homogenization of Fe, Mg, Ca, and Mn during any postgrowth thermal events was negligible. We use the zoning profiles with simple models of homogenization by volume diffusion to constrain the temperature-time history of these rocks. For a given radius and diffusion constant, the time required for an initial growth zoning profile (approximated by a normal curve) to relax by intragrain diffusion to 0.1 of its initial core-rim profile is given by

$$t = -r^2 \ln(0.1)/(1.43)^2 \pi^2 D \quad (1)$$

where t is time in seconds, r is the radius in metres, and D is the diffusion constant in m^2s^{-1}. The equation was derived by M. Hayashi (personal communication, 1999) from an equation given by Crank (1975). The garnet is assumed to represent a closed system. For a diffusion constant of 10^{-20} m^2s^{-1} (e.g., Spear, 1993, p. 613) and a radius of 1 x 10^{-3} m, the time required to homogenize the garnet is about 0.36 Myr. For a diffusion constant of 10^{-21} m^2s^{-1}, the time required increases to about 3.6 Myr. These estimates are compared to those yielded by the equation for "penetration by diffusion distance", given by

$$r = (Dt)^{1/2} \text{ (e.g., Spear, 1993, p. 613)} \quad (2)$$

For a diffusion constant of 10^{-20} m^2s^{-1}, it takes 0.32 Myr for an ion to diffuse over a distance of 1 x 10^{-3} m; this result is similar to those from the first model.

From these results, we conclude that any temperatures > ~500°C (i.e., those that yield diffusion constants of 10^{-20} - 10^{-21} m^2s^{-1}) after garnet growth in the samples with weakly zoned profiles cannot have been maintained for more than a few million years.

Weakly zoned profiles in sample 14 (domain 1) and samples 1 and 3 (domain 2) are interpreted as resulting from complete diffusional homogenization of Fe, Mg, Ca, and Mn. Such a process requires that the temperature in these samples were greater and (or) attained for longer times than those in samples with strongly zoned profiles (samples 9, 11, and 13). This is a predicted result given that the samples with weakly zoned profiles contain kyanite whereas those with strongly zoned profiles do not. An unpredicted result is the drastic difference in zoning

profiles in rocks from within domain 1. Perhaps differences in bulk composition are partly responsible.

Timing of metamorphism and deformation

The following data and interpretations are summarized in the timeline in Fig. 14.

Domain 1

Three periods of mineral growth were dated in domain 1, ~163, 90, and 70 Ma. Primary monazite and xenotime grew at ~163 Ma, which is the upper intercept of discordias defined by slightly to moderately discordant analyses (samples 9, 16, and 18) and roughly the age of the monazite cores (SHRIMP ages from sample 9). Although the age of primary monazite is underestimated by the upper intercept of a discordia defined by analyses with excess ^{206}Pb (i.e., the grains that were reversely discordant before an overprint), we conclude that that the primary monazite age is closely approximated by the 163 Ma upper intercept because xenotime, which does not contain excess ^{206}Pb, lies on the discordia. Secondary monazite growth in domain 1 occurred at 90 Ma (age of two concordant analyses in sample 22) and 67 ± 10 Ma (age of lower intercepts of discordias defined by monazite and xenotime from samples 9, 16, and 18, and age of monazite rims in sample 9). The scant petrographic evidence for multiple mineral growth events includes minor replacement of garnet and biotite by chlorite and chlorite overgrowth of S_{1+2}.

In order to properly determine the timing of the thermal peak of metamorphism, the growth of garnet (the peak index mineral in domain 1) in sample 9 must be correctly correlated with primary monazite growth at ~163 Ma or secondary growth at ~60 Ma. Garnet growth is interpreted as predating final S_{1+2} development because S_{1+2} is deflected around garnet, quartz-filled pressure shadows lie at the garnet margins, and garnet contains an inclusion fabric that predates S_{1+2} (Figs. 7, 8b, c). There are no constraints on the timing of S_{1+2} development in the immediate vicinity of sample 9, but 10 km to the south S_{1+2} was intruded by an undeformed 72.0 ± 0.5 Ma pegmatite dyke (sample 20). Assuming that S_{1+2} in the two localities is the same age, we conclude that S_{1+2} and garnet growth in sample 9 predates 72 Ma. Given that the only pre-72 Ma monazite growth in sample 9 occurred at ~163 Ma, garnet growth (i.e., peak metamorphism) is interpreted as occurring at ~163 Ma, roughly synchronous with pegmatite crystallization in domain 1 (samples 18 and 19).

The two periods of secondary monazite growth in domain 1 (~90 Ma in sample 22 and ~60 Ma in samples 9, 16, and 18) probably resulted from lower temperature events. The only constraint on temperature in the garnet schist comes from the fact that growth zoning in Fe, Mg, Ca, and Mn is preserved throughout garnet, which suggests that temperatures of ~500_C were not attained for a long enough time to cause diffusional homogenization. In contrast, similar or higher temperatures in kyanite-staurolite schist in domain 1 were attained for a long enough time to cause diffusional homogenization of garnet. The timing of staurolite and kyanite growth in this domain is unknown.

U-Pb dating of an undeformed pegmatite dyke (sample 20) indicates that deformation associated with S_{1+2} in domain 1 occurred before 72.0 ± 0.5 Ma. Two strongly deformed pegmatite layers (samples 18 and 19) yield imprecise crystallization ages of ~160 Ma, suggesting that deformation associated with S_{1+2} is younger than ~160 Ma.

Domain 2

The thermal peak in domain 2 occurred during kyanite growth. The youngest $^{208}Pb/^{232}Th$ SHRIMP age from a monazite inclusion in kyanite from sample 1 is 73.0 ± 1.3 Ma. Because this age is interpreted as representing monazite growth that predated kyanite, we conclude that kyanite grew during peak metamorphism at or since ~73 Ma. Kyanite may have grown a few million years after the monazite or it may have grown later, perhaps during formation of secondary monazite on the rim of a matrix grain at 66-60 Ma and (or) crystallization of a leucosome lens at 60.7 ± 0.5 Ma (sample 2). The presence of kyanite in the other leucosomes may indicate that depths suitable for kyanite growth were attained at ~61 Ma. Peak metamorphism occurred before crystallization of a postmetamorphic 58.4 ± 0.5 Ma pegmatite dyke (sample 4). Temperatures after garnet growth in domain 2 were high enough for a long enough time to cause diffusional homogenization of Fe, Mg, Ca, and Mn in garnet. We suggest that U-Pb ages from sample 3 indicate that ~160 Ma primary monazite underwent secondary growth at ~70 Ma. This interpretation requires that initial heating in domain 2 at ~160 Ma was coeval with peak metamorphism in domain 1, during which time the cores of the garnets in domain 2 may have grown. The only constraint on garnet growth, from SHRIMP spot ages in monazite inclusions, is that the rims postdate 110 Ma.

Part of the S_{1+2} development in domain 2 occurred after crystallization of a 63.5 ± 0.5 Ma deformed pegmatite layer (sample 24) and a 60.7 ± 0.5 Ma leucosome lens (sample 2). It cannot be ruled out that most of S_{1+2} development occurred before these times and that deformation after these times occurred on a reactivated S_{1+2}. S_{1+2} development ceased before crystallization of a 58.4 ± 0.5 Ma undeformed pegmatite dyke (sample 4). Postmetamorphic (F_3) folding associated with the Mica Creek antiform is thus bracketed between 60.7 ± 0.5 and 58.4 ± 0.5 Ma.

Domain 3

The thermal peak in domain 3 occurred during sillimanite and kyanite growth, the ages of which are poorly constrained by our dating; the only firm constraint is that growth occurred before crystallization of a 62.7 ± 0.5 Ma postmetamorphic pegmatite dyke (sample 7). Growth most likely occurred during one of the five periods of monazite growth that were dated in three schists and one metamorphosed leucogranite (Fig. 14). Most grains grew at 99-93 Ma and many >99 Ma grains underwent substantial secondary growth then. Grains that are >99 Ma include three that grew during the 166-160 Ma metamorphism that greatly affected domain 1, three that grew during the 110 Ma event represented by monazite inclusions in garnet in domain 2, and two that grew in the Permian. In addition, one grain grew during the 70 Ma event that greatly affected domain 2 and two older grains underwent overgrowth or recrystallization at ~70 Ma. Given the predominance of monazite growth at 99-93 Ma (Fig. 14) and the fact that large monazites in thin section appear to be part of the peak metamorphic assemblage (i.e., they lie

within S_{1+2} in contact with kyanite (Fig. 8h)), we suggest that peak metamorphism occurred at 99-93 Ma. The significance of the Permian monazite domains is unknown, yet it is certain they are not detrital because the protolith was deposited in the Neoproterozoic.

Part of the S_{1+2} development in domain 3 occurred after crystallization of a 122 ± 1 Ma leucogranite (sample 6) and before crystallization of a 62.7 ± 0.5 Ma undeformed pegmatite dyke (sample 7).

Summary of timing

Our interpretations of the U-(Th)-Pb data lead to two important conclusions concerning the timing of metamorphism in the Mica Creek area. First, the thermal peak of metamorphism occurred at different times in each of the three age domains (Fig. 14). In domain 1 it occurred at ~163 M, in domain 2 it occurred between ~73 and 58 Ma, possibly at ~61 Ma, and in domain 3 it occurred at 99-93 Ma. Second, the domains were affected by numerous secondary thermal events, many of which are coeval with peak metamorphism in other domains (Fig. 14). For example, domain 1 was affected by 90 and 60 Ma events that are coeval with peak metamorphism in domains 3 and 2, respectively. Domain 3 was affected by ~160 and 70 Ma events that are coeval with peak metamorphism in domains 1 and 2, respectively. Secondary events at 110 Ma occurred in domains 2 and 3.

Our interpretations of the U-Pb data from the intrusive rocks (Fig. 14) and their structural relationships require that deformation responsible for S_{1+2} occurred before 72.0 ± 0.5 Ma in domain 1, whereas in domain 2 at least part of it occurred between 60.7 ± 0.5 and 58.4 ± 0.5 Ma. Equivalent deformation in domain 3 occurred before 62.7 ± 0.5 Ma, before part of this deformation in domain 2 and possibly during this deformation in domain 1. It cannot be ruled out that relatively young deformation in domain 2 reactivated a foliation that developed throughout the Mica Creek area as early as 160 Ma.

Tectonic implications

The U-(Th)-Pb dating indicates that tectonism occurred in parts of the Mica Creek area at ~163, 122, 110, 99-93, and 72-58 Ma (Fig. 14), roughly coincident with the five recognized major periods of metamorphism, deformation, and plutonism in the metamorphic core of the southeastern Canadian Cordillera (Parrish, 1995 and references therein). There are many regions in the Cordillera that underwent tectonism during two or three of these periods, but the Mica Creek area is the only known region that was tectonized during all five.

Given that the Mica Creek area contains metamorphic zones and structural elements that cross from the northern Selkirk Mountains through the northern Monashees into the Cariboos without the interruption of faults with large displacements, it is not surprising that the area experienced the 175-160 Ma tectonism typical of the northern Selkirks and the 100-90 and 70-60 Ma tectonism typical of the northern Monashees. In particular, metamorphism and pegmatite emplacement at ~163 Ma in domain 1 were synchronous with tectonism in the northern Selkirks (Shaw, 1980; Archibald et al., 1983; Brown et al., 1992, Colpron et al., 1996). Leucogranite crystallization at 122 Ma in domain 3 followed shortly after metamorphism in the northernmost

Monashees (J.H. Sevigny, unpublished data, 1992). The thermal event at 110 Ma in domains 2 and 3 was synchronous with pegmatite crystallization in the northern Monashees (Parrish, 1995) and crystallization of the protolith of two orthogneisses in the Valhalla complex (Parrish et al., 1988; Parrish, 1995; Spear and Parrish, 1996). Metamorphism at 99-93 Ma in domain 3 was synchronous with leucogranite crystallization and metamorphism in the northern Monashees (Sevigny et al., 1989; Scammell, 1993), leucogranite crystallization (Anstey pluton) on the west flank of the northern Monashee complex (Parrish, 1995), and post-deformational plutonism in the Selkirks (Archibald et al., 1983; Crowley and Brown, 1994). Metamorphism, deformation, and pegmatite crystallization at 72-58 Ma in domain 2 were synchronous with leucogranite crystallization (Sevigny et al., 1989; Scammell, 1993) and a localized sillimanite overprint in the northern Monashees (Digel et al., 1998), and metamorphism in the Monashee (Parrish, 1995; Crowley and Parrish, 1999; Gibson et al., 1999) and Valhalla complexes (Heaman and Parrish, 1991; Spear and Parrish, 1996). Timing in the Valhalla complex is similar to that in the Mica Creek area; it underwent plutonism at 165 and 110 Ma, high-grade metamorphism at 70 Ma, and leucogranite and pegmatite crystallization at 58-54 Ma. The Clachnacudainn complex is another region with a multi-episodic history, with granitoid intrusion occurring in the Devonian, probably Middle Jurassic, mid-Cretaceous, Late Cretaceous, and probably Paleocene (Crowley and Brown, 1994 and references therein).

Our interpreted metamorphic ages in the Mica Creek area, although consistent with ages obtained throughout the SMC complex, are inconsistent with a simple interpretation of the continuous metamorphic sequence that was mapped by Simony et al. (1980) (Figs. 2, 3). The continuous sequence was, for example, taken by Ghent et al. (1980) and Digel et al. (1998) to imply that all index minerals grew in the same metamorphic event. Our dating indicates that garnet in the garnet zone grew 100 Myr before kyanite in the adjacent kyanite-migmatite zone, and this kyanite grew 25 Myr after some of the sillimanite in the adjacent sillimanite-migmatite zone. In addition, the timing constraints on deformation may indicate a more complex deformation history than that interpreted by Simony et al. (1980) (Figs. 2, 3). Their interpretation holds that a continuous train of folds (Simony et al., 1980; Raeside and Simony, 1983) formed in one F_2 folding event that was associated a widespread S_{1+2}, whereas our dating shows that F_2 folding in domain 1 occurred >10 Myr before some S_{1+2} development in domain 2.

The key to understanding the tectonic history of the Mica Creek area and the SMC complex is determining why several metamorphic and deformation events spanning 100 Myr occurred in a single tectonometamorphic complex with apparent metamorphic, deformation, and stratigraphic continuity. We propose two explanations. First, the continuity is only apparent, with the metamorphic and deformation elements of disparate ages having been tectonically assembled along cryptic, unrecognized shear zones. Second, the continuity is correctly interpreted from the mapping, but it is the result of thermal and deformation events superimposed locally on the complex.

In polymetamorphosed and polydeformed rocks, it is difficult to prove that presently adjacent rocks were adjacent throughout their history. Modeling by Jamieson et al. (1996) showed that an apparently continuous metamorphic sequence could form by tectonic juxtaposition of rocks that had widely varying initial positions and reached peak temperatures at different times and places in the orogen. If the geologic continuity in the Mica Creek area is apparent rather than real, it is

possible that the three age domains identified in this study were tectonized, at least in part, at different times and places in the orogen and then assembled into their present positions via cryptic structures that have not been recognized. Such structures, which must be relatively young features, could include broad foliation-parallel zones of intense transposition and shear, as well as distinct faults. The fact that the stratigraphic succession in the study area (Figs. 2, 3) includes zones of monotonous pelitic and semipelitic schists that could belong to several stratigraphic units makes it difficult to be certain that the apparent stratigraphic continuity precludes major displacements between the domains.

The boundary between domains 1 and 2 could be a shear zone that lies within platy semipelitic schist to the northeast of Mount Nagle, following S_{1+2} to the northwest and southeast. At the transverse fault in Kinbasket Lake (Fig. 2), the boundary would show a ~1 km sinistral strike separation and continue to the east-southeast near the shore of the lake. The boundary between domains 2 and 3 could be a shear zone that follows S_{1+2} between Nagle Creek and sample 28 (Fig. 2). It would underlie Mica Creek Village, on the north or south (position shown on Fig. 2) limb of the synform that passes through the village. If the north limb option were correct, the shear zone would be folded over the F_3 Mica Dam antiform (Simony et al., 1980) and join the boundary between domains 1 and 2 near the east side of the study area.

The proposed shear zones between the age domains are plausible because they lie in sheared and transposed rocks and do not cross identified marker horizons. The question remains, however, whether such zones have sufficient translation to explain our tectonic dilemma. The following observations suggest that the domains were never greatly separated. The domains contain the same stratigraphic units. The shared periods of monazite growth between the domains (Fig. 14) suggest that they have similar thermal histories. Metamorphic mineral assemblages in adjacent domains belong to the same bathozone (Carmichael, 1978), suggesting that different crustal levels were not juxtaposed. Detailed mapping along the domain boundaries is required to refute or confirm the possibility that the boundaries are shear zones and that the age domains were tectonically assembled.

If translation along the domain boundaries was not large, we must consider the alternate explanation that episodes of regional metamorphism and granitoid intrusion occurred in elongate zones bounded by steeply dipping isothermal surfaces with high lateral thermal gradients. These zones of metamorphism and intrusion must have formed at different times in different portions of the SMC complex. We recognize that this explanation also leaves unresolved problems. For example, heating at 72-58 Ma in domain 2 was sufficient for kyanite growth, yet it had no effect on garnet zoning in adjacent portions of domain 1. Moreover, heating at 99-93 Ma in domain 3 was sufficient for kyanite and sillimanite growth, yet it did not result in any monazite growth in adjacent parts of domain 2. Granitic plutons of the proper age that could have been effective local sources of heat and pegmatitic fluid have not been identified.

We propose the following possible tectonic history for the SMC complex in the Mica Creek area:

>170-160 Ma: Large, west-verging nappe structures, like the Scrip Nappe, formed and a cleavage (S_1) developed at low metamorphic grade.
170-160 Ma: Earliest structures were deformed by F_2 folds and an axial planar foliation (S_{1+2}) formed. Metamorphism was at garnet grade, locally reaching staurolite and kyanite grade. The rocks cooled shortly after metamorphism. The metamorphic assemblages and S_{1+2} were only preserved from younger tectonism in domain 1.
140-120 Ma: Kyanite- and sillimanite-grade metamorphism occurred in the northernmost part of the SMC complex (north of domain 1). Leucogranites intruded locally.
110 Ma: A low grade metamorphic event occurred in domains 2 and 3.
100-90 Ma: Kyanite- and sillimanite-grade metamorphism occurred in domain 3 and rocks to the southwest. Amount of deformation during this time is unknown. Leucogranite intrusion was abundant to the southwest of domain 3.
75-60 Ma: Leucogranite intrusion, kyanite- and sillimanite-grade metamorphism, and deformation occurred in domain 2, coincident with thrusting of the SMC complex over the Monashee complex. Late-stage pegmatites and fluids infiltrated all domains.

In this scenario, the apparently continuous metamorphic sequence in the SMC complex largely resulted from a combination of mineral growth at 170-160, 140-120, 100-90, and 75-60 Ma, with some of the events occurring in all the rocks and others having local effects. Although it is unlikely that the growth events occurred when the rocks were in their present relative positions, it is difficult to envision that they occurred when the rocks were widely separated. The relatively simple pattern of a train of large F_2 folds with a southwest-dipping S_{1+2} axial planar foliation may have been first established at 170-160 Ma and this orientation was preserved through younger periods of deformation, possibly because S_{1+2} was oriented such that it was reactivated and recrystallized while only being mildly folded.

The structural position of the SMC complex in the Cordillera, below the accreted terranes and above the autochthonous Paleoproterozoic basement (Monashee complex), may explain why it was affected by multiple tectonometamorphic events. The accreted terranes were deformed and metamorphosed during and shortly after accretion in the Early Jurassic then uplifted to high structural levels. The basement rocks were at high structural levels until they were buried in the Late Cretaceous-Early Tertiary under an easterly advancing SMC complex and Rocky Mountain Foreland Belt relatively late in the Cordilleran orogenesis (Parrish, 1995; Crowley and Parrish, 1999). In contrast, the intermediate structural position occupied by the SMC complex allowed it to be heated and deformed during numerous intervening orogenic events.

Acknowledgments

This work was supported by Natural Sciences and Engineering Research Council of Canada (NSERC) research grants to EDG, PSS, and SDC. This is Geological Survey of Canada Contribution Number 2000028. J.P. Crowley and S.E. Crowley assisted with field work. The Geological Survey of Canada in Calgary provided use of their scanning electron microscope, with which we were assisted by J. Wong. J. Resultay prepared grain mounts. P. Gromet and W. Trzcienski are thanked for constructive reviews.

References

Archibald, D.A., Glover, J.K., Price, R.A., Farrar, E., and Carmichael, D.M. (1983) Geochronology and tectonic implications of magmatism and metamorphism, southern Kootenay arc and neigbouring regions, southeastern British Columbia. Part I: Jurassic to mid-Cretaceous. Canadian Journal of Earth Sciences, 20, 1891-1913.

Bence, A.E., and Albee, A.L. (1968) Empirical correction factors for the electron microanalysis of silicates and oxides. Journal of Geology, 76, 382-403.

Brown, R.L., McNicoll, V.J., Parrish, R.R., and Scammell, R.J. (1992) Middle Jurassic plutonism in the Kootenay Terrane, northern Selkirk Mountains, British Columbia. In Radiogenic age and isotopic studies, Report 5, Geological Survey of Canada Paper, 91-2, 135-141.

Carr, S.D. (1995) The southern Omineca Belt, British Columbia: new perspectives from the Lithoprobe Geoscience Program. Canadian Journal of Earth Sciences, 32, 1720-1739.

Carmichael, D. M. (1978) Metamorphic bathozones and bathograds: a measure of post-metamorphic uplift and erosion on a regional scale. American Journal of Science, 278, 769-797.

Colpron, M., Price, R.A., Archibald, D.A., and Carmichael, D.M. (1996) Middle Jurassic exhumation along the western flank of the Selkirk fan structure: Thermobarometric and thermochronometric constraints from the Illecillewaet synclinorium, southeastern British Columbia. Geological Society of America Bulletin, 108, 1372-1392.

Crank, J. (1975) The Mathematics of Diffusion, Second Edition. Oxford University Press, 414p.

Crowley, J.L., and Brown, R.L. (1994) Tectonic links between the Clachnacudainn terrane and Selkirk allochthon, southern Omineca Belt, Canadian Cordillera. Tectonics, 13, 1035-1051.

Crowley, J.L., Parrish, R.R. (1999) U-Pb isotopic constraints on diachronous metamorphism of variable intensity in the northern Monashee complex, southern Canadian Cordillera. Journal of Metamorphic Geology, 17, 483-502.

Crowley, J.L., and Ghent, E.D. (1999) An electron microprobe study of the U-Th-Pb systematics of metamorphosed monazite: the role of Pb diffusion versus overgrowth and recrystallization. Chemical Geology, 157, 285-302.

Digel, S.G., Ghent, E.D., Carr, S.D., and Simony, P.S. (1998) Early Cretaceous kyanite-sillimanite metamorphism and Paleocene sillimanite overprint near Mount Cheadle, southeastern British Columbia: geometry, geochronology, and metamorphic interpretations. Canadian Journal of Earth Sciences, 35, 1070-1087.

Gerasimoff, M.D. (1988) The Hobson Lake pluton, Cariboo Mountains, and its significance to Mesozoic and Early Tertiary Cordilleran tectonics, MSc thesis, Queen's University, Kingston, Ontario.

Ghent, E.D., and Valley, J.W. (1998) Oxygen isotope study of quartz-Al_2SiO_5 pairs from the Mica Creek area, British Columbia: implications for the recovery of peak metamorphic temperatures. Journal of Metamorphic Geology, 16, 223-230.

Ghent, E.D., Knitter, C.C., Raeside, R.P., and Stout, M.Z. (1982) Geothermometry and geobarometry of pelitic rocks, upper kyanite and sillimanite zones, Mica Creek area, British Columbia. Canadian Mineralogist, 20, 295-305.

Ghent, E.D., Stout, M.Z., and Raeside, R.P. (1983) Plagioclase-clinopyroxene-garnet-quartz-equilibria and the geobarometry and geothermometry of garnet amphibolites from, Mica Creek, British Columbia. Canadian Journal of Earth Sciences, 20, 699-706.

Gibson, H.D., Brown, R. L., and Parrish, R.R. (1999) Deformation-induced inverted metamorphic field gradients: an example from the southeastern Canadian Cordillera. Journal of Structural Geology, 21, 751-767.

Heaman, L., and Parrish, R. (1991) U-Pb geochronology of accessory minerals. In Heaman, L., and Ludden, J.N., Eds., Applications of Radiogenic Isotope Systems to Problems in Geology, Short Course 19, 59-102, Mineralogical Association of Canada.

Jamieson, R.A., Beaumont, C., Hamilton, J., and Fullsack, P. (1996) Tectonic assembly of inverted metamorphic sequences. Geology, 24, 839-842.

Kretz, R. (1983) Symbols for rock forming minerals. American Mineralogist, 68, 277-279.

Krogh, T.E. (1982) Improved accuracy of U-Pb ages by the creation of more concordant systems using an air abrasion technique. Geochimica et Cosmochimica Acta, 46**,** 637-649.

McDonough, M.R. (compiler), Simony, P.S., Sevigny, J.H., Robbins, D.B., Raeside, R., Doucet, P., Pell, J., and Dechesne, R.G. (1992) Geology of Nagle Creek and Blue River, British Columbia (83D/2 and 83D/3). Geological Survey of Canada, Open File 2512, scale 1 : 50,000.

Monger, J.W.H., Price, R.A., and Tempelman-Kluit, D.J. (1982) Tectonic accretion and the origin of the two major metamorphic and plutonic welts in the Canadian Cordillera. Geology, 10, 70-75.

Nicholls, J. and Stout, M.Z. (1986) Electron beam analytical instruments and the determination of modes, spatial variations of minerals and textural features of rocks in polished section. Contributions to Mineralogy and Petrology, 94, 395-404.

Parrish, R.R. (1987) An improved micro-capsule for zircon dissolution in U-Pb geochronology. Chemical Geology, 66, 99-102.

Parrish, R.R. (1990) U-Pb dating of monazite and its applications to geological problems, Canadian Journal of Earth Sciences, 27, 1431-1450.

Parrish, R.R. (1995) Thermal evolution of the southeastern Canadian Cordillera. Canadian Journal of Earth Sciences, 32, 1618-1642.

Parrish, R.R., and Krogh, T.E. (1987) Synthesis and purification of ^{205}Pb for U-Pb geochronology. Chemical Geology, 66, 103-110.

Parrish, R.R., Roddick, J.C., Loveridge, W.D., and Sullivan, R.W. (1987) Uranium-lead analytical techniques at the Geochronology Laboratory. In Radiogenic age and isotopic studies, Report 1, Geological Survey of Canada Paper, 87-2, 3-7.

Parrish, R.R., Carr, S.D., and Parkinson, D.L. (1988) Eocene extensional tectonics and geochronology of the southern Omineca Belt, British Columbia and Washington. Tectonics, 7, 181-212.

Pell, J. and Simony, P.S. (1987) New correlations of Hadryian strata, south-central British Columbia. Canadian Journal of Earth Sciences, 24, 303-313.

Raeside, R.P. and Simony, P.S. (1983) Stratigraphy and deformational history of the Scrip Nappe, Monashee Mountains, British Columbia. Canadian Journal of Earth Sciences, 20, 639-650.

Read, P.B., Woodsworth, G.J., Greenwood, H.J., Ghent, E.D., and Evenchick, C.A. (1991) Metamorphic map of Canadian Cordillera. Geological Survey of Canada Map 1714A, scale 1 : 2,000,000.

Roddick, J.C. (1987) Generalized numerical error analysis with applications to geochronology and thermodynamics. Geochimica et Cosmochimica Acta, 51**,** 2129-2135.

Roddick, J.C., Loveridge, W.D., and Parrish, R.R. (1987) Precise U/Pb dating of zircon at the sub-nanogram Pb level. Chemical Geology, 66, 111-121.

Scammell, R.J. (1993) Mid-Cretaceous to Tertiary thermotectonic history of former mid-crustal rocks, southern Omineca Belt, Canadian Cordillera. PhD thesis, Queen's University, Kingston, Ontario.

Schärer, U. (1984) The effect of initial ^{230}Th disequilibrium on young U-Pb ages: the Makalu case, Himalaya. Earth and Planetary Science Letters, 67, 191-204.

Sevigny, J.H, Parrish, R.R., and Ghent, E.D. (1989) Petrogenesis of peraluminous granite, Monashee Mountains, southeastern Canadian Cordillera. Journal of Petrology, 30, 557-581.

Sevigny, J.H, Parrish, R.R., Donelick, R.A. and Ghent, E.D. (1990) Northern Monashee Mountains, Omineca Crystalline Belt, British Columbia: Timing of metamorphism, anatexis, and tectonic denudation. Geology, 18, 103-106.

Shaw, D. (1980) A concordant uranium-lead age for zircons in the Adamant pluton, British Columbia. In Current Research, Part C, Geological Survey of Canada, 80-1C, 243-246.

Simony, P.S., Ghent, E.D., Craw, D., Mitchell, W., and Robbins, D.B. (1980) Structural and metamorphic evolution of northeast flank of Shuswap complex, southern Canoe River area, British Columbia. Geological Society of America, Memoir 153, 445-461.

Spear, F.S. (1993) Metamorphic phase equilibria and pressure-temperature-time paths. Mineralogical Society of America Monograph, 789 p.

Spear, F.S., and Parrish, R.R. (1996) Petrology and cooling rates of the Valhalla complex, British Columbia, Canada. Journal of Petrology, 37, 733-765.

Steiger, R.H., and Jäger, E. (1977) Subcommision on geochronology: convention on the use of decay constants in geo- and cosmochronology. Earth and Planetary Science Letters, 36, 359-362.

Stern, R.A. (1997) The GSC Sensitive High Resolution Ion Microprobe (SHRIMP): analytical techniques of zircon U-Th-Pb age determination and performance evaluation. In Radiogenic Age and Isotopic Studies: Report 10; Geological Survey of Canada, Current Research 1997-F, 1-31.

Stern, R.A., and Sanborn, N. (1998) Monazite U-Pb and Th-Pb geochronology by high-resolution secondary ion mass spectrometry. In Radiogenic Age and Isotopic Studies: Report 11; Geological Survey of Canada, Current Research 1998-F, 1-18.

Stout, M.Z., Crawford, M.L., and Ghent, E.D. (1986) Pressure-temperature and evolution of fluid compositions of Al_2SiO_5-bearing rocks, Mica Creek, B.C., in light of fluid inclusion data and mineral equilibria. Contributions to Mineralogy and Petrology, 92, 236-247.

York, D. (1969) Least squares fitting of a straight line with correlated errors. Earth and Planetary Science Letters, 5, 320-324.

Table 1. U-Pb IDTIMS analytical data.

Analysis[a]	Weight[b] (µg)	U (ppm)	Pb*[c] (ppm)	$^{206}Pb/^{204}Pb$[d]	Pb_c[e] (pg)	^{208}Pb (%)[f]	$^{206}Pb/^{238}U$[g]	$^{207}Pb/^{235}U$[g]	$^{207}Pb/^{235}U$ age[h] (Ma)	Correlation coefficient	$^{207}Pb/^{206}Pb$[g]	$^{207}Pb/^{206}Pb$ age[h] (Ma)
Sample 9. (MC-09-97) (Fig. 5a). Garnet schist in domain 1; head of Franchère Creek at 2200 m, 392540E-5785600N												
1	149	20	3751	173	8149	14	52.3	0.024330 ± 0.12%	0.16520 ± 0.12%	155.2 ± 0.3	0.84	0.04925 ± 0.07%	159.6 ± 3.4
2	105	8	4555	207	5343	9	58.8	0.020621 ± 0.10%	0.13937 ± 0.12%	132.5 ± 0.3	0.84	0.04902 ± 0.06%	148.7 ± 3.1
3	105	4	7765	603	2485	20	70.7	0.025055 ± 0.11%	0.17011 ± 0.13%	159.5 ± 0.4	0.79	0.04924 ± 0.08%	159.3 ± 4.2
4	105	4	5569	345	3249	8	71.7	0.019326 ± 0.09%	0.13018 ± 0.13%	124.3 ± 0.3	0.75	0.04885 ± 0.09%	140.8 ± 4.3
Sample 16. (MC-16-97) (Fig. 4a). Biotite schist in domain 1; head of north branch of Encampment Creek at 2080m, 388900E-5781460N												
1	149	21	17723	563	57940	10	32.4	0.023741 ± 0.12%	0.16101 ± 0.13%	151.6 ± 0.4	0.97	0.04919 ± 0.03%	156.8 ± 1.4
X1	149	41	13823	308	79484	11	3.2	0.023939 ± 0.16%	0.16243 ± 0.17%	152.8 ± 0.5	0.99	0.04921 ± 0.03%	157.9 ± 1.3
X2	149	11	18863	414	41829	7	3.7	0.023417 ± 0.10%	0.15872 ± 0.11%	149.6 ± 0.3	0.97	0.04916 ± 0.03%	155.4 ± 1.4
X3	149	13	11109	228	30109	7	3.4	0.022021 ± 0.11%	0.14894 ± 0.12%	141.0 ± 0.3	0.95	0.04905 ± 0.04%	150.4 ± 1.6
Sample 18. (MC-18-97) (Fig. 6a, b). Deformed pegmatite layer in domain 1; head of north branch of Encampment Creek at 2080m, 388900E-5781460N												
A	149	9	264	16	173	27	59.6	0.027544 ± 0.24%	0.20241 ± 1.5%	187.2 ± 5.2	0.56	0.05330 ± 1.4%	341.5 ± 63.7
B	149	8	183	34	419	23	49.5	0.099469 ± 0.17%	1.09686 ± 0.46%	751.8 ± 4.8	0.55	0.07998 ± 0.39%	1196.4 ± 15.4
C	149	6	331	16	498	7	53.7	0.025096 ± 0.17%	0.18375 ± 0.64%	171.3 ± 2.0	0.48	0.05310 ± 0.58%	333.2 ± 26.4
D	149	5	83	8	255	4	67.2	0.033059 ± 0.63%	0.64662 ± 0.87%	506.4 ± 6.9	0.79	0.14186 ± 0.54%	2250.0 ± 18.5
1	202	41	1914	189	1551	63	82.1	0.019442 ± 0.10%	0.13058 ± 0.16%	124.6 ± 0.4	0.76	0.04871 ± 0.10%	133.9 ± 4.9
2	202	31	3225	117	1137	65	71.6	0.011344 ± 0.11%	0.07436 ± 0.19%	72.8 ± 0.3	0.70	0.04754 ± 0.14%	76.5 ± 6.6
3	149	20	2974	113	1182	44	67.9	0.013450 ± 0.14%	0.08896 ± 0.20%	86.5 ± 0.3	0.65	0.04797 ± 0.15%	97.7 ± 7.2
Sample 19. (MC-19-97) (Fig. 6c). Deformed pegmatite layer in domain 1; head of a south branch of Encampment Creek, northeast of Mount Nagle at 1880 m, 392080E-5775400N												
A	149	18	5162	772	32750	28	0.1	0.161818 ± 0.10%	1.65176 ± 0.11%	990.2 ± 1.4	0.97	0.07403 ± 0.03%	1042.3 ± 1.2
B	149	12	7082	889	37266	20	0.1	0.135975 ± 0.09%	1.37006 ± 0.10%	876.2 ± 1.2	0.96	0.07308 ± 0.03%	1016.1 ± 1.2
C	149	12	6094	889	18492	39	0.1	0.157817 ± 0.09%	1.60735 ± 0.10%	973.1 ± 1.3	0.96	0.07387 ± 0.03%	1037.8 ± 1.2
D	105	3	3304	510	2590	39	0.2	0.166969 ± 0.09%	1.70585 ± 0.11%	1010.7 ± 1.4	0.87	0.07410 ± 0.06%	1044.1 ± 2.3
E	105	2	8239	1297	15330	11	0.4	0.169940 ± 0.09%	1.72359 ± 0.10%	1017.4 ± 1.3	0.94	0.07356 ± 0.03%	1029.4 ± 1.4
Sample 20. (MC-20-97) (Fig. 6d). Undeformed pegmatite dyke in domain 1; head of a south branch of Encampment Creek, northeast of Mount Nagle at 1880 m, 392080E-5775400N												
1	202	39	13881	524	2052	203	71.4	0.011939 ± 0.15%	0.07325 ± 0.18%	71.8 ± 0.3	0.89	0.04450 ± 0.09%	-83.1 ± 4.2
2	202	24	30241	588	3527	151	46.7	0.011467 ± 0.28%	0.07368 ± 0.29%	72.2 ± 0.4	0.98	0.04660 ± 0.05%	28.9 ± 2.5
3	202	19	13579	514	2226	90	71.3	0.012005 ± 0.12%	0.07347 ± 0.15%	72.0 ± 0.2	0.86	0.04439 ± 0.08%	-89.2 ± 3.8

Table 1. (*continued*).

Analysis[a]	Weight[b] (μg)	U (ppm)	Pb*[c] (ppm)	$^{206}Pb/^{204}Pb$[d]	Pb_c[e] (pg)	^{208}Pb (%)[f]	$^{206}Pb/^{238}U$[g]	$^{207}Pb/^{235}U$[g]	$^{207}Pb/^{235}U$ age[h] (Ma)	Correlation coefficient	$^{207}Pb/^{206}Pb$[g]	$^{207}Pb/^{206}Pb$ age[h] (Ma)
Sample 22. (MC-22-97) (Fig. 4b). Garnet schist in domain 1; head of a south branch of Encampment Creek, northeast of Mount Nagle at 1810 m, 392460E-5775560N												
1	149	18	6903	492	7841	25	68.2	0.024987 ± 0.10%	0.16974 ± 0.11%	159.2 ± 0.3	0.94	0.04927 ± 0.04%	160.7 ± 1.8
2	149	9	8644	346	4054	17	68.5	0.013917 ± 0.10%	0.09176 ± 0.12%	89.1 ± 0.2	0.91	0.04782 ± 0.05%	90.3 ± 2.6
3	149	7	10062	353	5172	12	63.5	0.014168 ± 0.11%	0.09347 ± 0.12%	90.7 ± 0.3	0.82	0.04785 ± 0.07%	91.7 ± 3.1
4	105	4	10180	705	5807	11	69.2	0.023493 ± 0.09%	0.15924 ± 0.11%	150.0 ± 0.3	0.89	0.04916 ± 0.05%	155.5 ± 2.3
Sample 1. (MC-01-97) (Fig. 5b). Migmatitic kyanite schist in domain 2; roadcut on Highway 23, 0.5 km south of Mica Dam at 740 m, 393180E-5770260N												
1	149	20	9263	300	962	144	67.8	0.011508 ± 0.12%	0.07539 ± 0.22%	73.8 ± 0.3	0.74	0.04752 ± 0.16%	75.3 ± 7.4
2	149	14	8260	280	812	104	70.2	0.011181 ± 0.12%	0.07225 ± 0.25%	70.8 ± 0.3	0.67	0.04687 ± 0.19%	42.6 ± 9.0
3	149	14	13060	340	791	167	61.7	0.011022 ± 0.12%	0.07118 ± 0.26%	69.8 ± 0.3	0.72	0.04684 ± 0.19%	40.9 ± 9.0
4	149	10	13689	432	1569	67	66.1	0.011822 ± 0.10%	0.07769 ± 0.16%	76.0 ± 0.2	0.81	0.04766 ± 0.10%	82.4 ± 4.8
5	149	8	14176	493	1579	55	68.8	0.011954 ± 0.11%	0.07864 ± 0.16%	76.9 ± 0.2	0.80	0.04714 ± 0.10%	85.1 ± 4.7
Sample 2. (MC-02-97) (Fig. 6e). Deformed leucosome lens in domain 2; roadcut on Highway 23, 0.5 km south of Mica Dam at 740 m, 393180E-5770260N												
A	149	9	11953	103	1343	49	0.1	0.009539 ± 0.10%	0.06249 ± 0.26%	61.6 ± 0.2	0.53	0.04751 ± 0.23%	75.0 ± 10.7
B	149	6	11251	97	2985	14	0.2	0.009517 ± 0.09%	0.06209 ± 0.18%	61.2 ± 0.2	0.64	0.04732 ± 0.14%	65.2 ± 6.7
1	202	21	37247	513	2508	195	36.2	0.009742 ± 0.23%	0.06169 ± 0.25%	60.8 ± 0.3	0.96	0.04593 ± 0.07%	-6.1 ± 3.6
2	202	17	42823	583	2096	217	35.7	0.009709 ± 0.21%	0.06155 ± 0.23%	60.6 ± 0.3	0.94	0.04598 ± 0.08%	-3.6 ± 4.0
Sample 3. (MC-03-97) (Fig. 4c). Migmatitic kyanite schist in domain 2; roadcut at Potlatch Creek at 780 m, 395540E-5772320N												
1	149	9	15506	750	5225	33	63.8	0.019313 ± 0.14%	0.12939 ± 0.14%	123.5 ± 0.3	0.75	0.04859 ± 0.10%	128.1 ± 4.6
2	105	8	11529	521	5499	21	59.9	0.020009 ± 0.10%	0.13410 ± 0.12%	127.8 ± 0.3	0.92	0.04861 ± 0.05%	129.1 ± 2.3
3	149	16	18383	1031	6922	53	68.3	0.019598 ± 0.13%	0.13164 ± 0.14%	125.6 ± 0.3	0.96	0.04872 ± 0.04%	134.2 ± 1.7
4	105	5	18258	939	6204	19	63.5	0.020735 ± 0.09%	0.13906 ± 0.11%	132.2 ± 0.3	0.92	0.04864 ± 0.04%	130.5 ± 2.0
Sample 4. (MC-04-97) (Fig. 6e). Undeformed pegmatite dyke in domain 2; top of Mica Dam spillway at 800 m, 393180E-5771040N												
1	149	13	35054	397	2342	116	26.2	0.009279 ± 0.18%	0.05905 ± 0.21%	58.3 ± 0.2	0.93	0.04615 ± 0.08%	5.7 ± 3.6
2	149	10	33655	391	2027	99	28.1	0.009283 ± 0.15%	0.05899 ± 0.18%	58.2 ± 0.2	0.74	0.04609 ± 0.12%	2.3 ± 5.9
3	105	7	46044	508	2406	80	24.6	0.009226 ± 0.13%	0.05938 ± 0.18%	58.6 ± 0.2	0.81	0.04668 ± 0.10%	32.9 ± 5.0

Table 1. (*continued*).

Analysis[a]	Weight[b] (μg)	U (ppm)	Pb*[c] (ppm)	$^{206}Pb/^{204}Pb$[d]	Pb_c[e] (pg)	^{208}Pb (%)[f]	$^{206}Pb/^{238}U$[g]	$^{207}Pb/^{235}U$[g]	$^{207}Pb/^{235}U$ age[h] (Ma)	Correlation coefficient	$^{207}Pb/^{206}Pb$[g]	$^{207}Pb/^{206}Pb$ age[h] (Ma)
Sample 24. (MC-24-97) (Fig. 6f). Deformed pegmatite layer in domain 2; shore of Kinbasket Lake, 0.75 km west of Potlatch Creek at 760 m, 394800E-5772420N												
1	149	28	16883	329	1906	167	51.8	0.010413 ± 0.23%	0.06444 ± 0.28%	63.4 ± 0.3	0.92	0.04488 ± 0.11%	-62.1 ± 5.5
2	149	17	17007	392	1945	100	59.0	0.010451 ± 0.18%	0.06579 ± 0.21%	64.7 ± 0.3	0.85	0.04566 ± 0.11%	-20.4 ± 5.4
3	149	9	17058	400	2184	49	58.2	0.010847 ± 0.13%	0.06956 ± 0.17%	68.3 ± 0.2	0.86	0.04651 ± 0.09%	24.1 ± 4.3
4	149	7	22217	578	1577	70	61.9	0.010959 ± 0.12%	0.07014 ± 0.22%	68.8 ± 0.3	0.61	0.04642 ± 0.18%	19.3 ± 8.5
5	149	15	20586	402	2427	84	52.4	0.010311 ± 0.13%	0.06444 ± 0.15%	63.4 ± 0.2	0.85	0.04533 ± 0.08%	-38.1 ± 3.9
6	149	15	20527	405	2101	97	52.9	0.010312 ± 0.14%	0.06459 ± 0.18%	63.6 ± 0.2	0.85	0.04543 ± 0.10%	-32.6 ± 4.8
7	105	7	24953	580	1868	61	60.7	0.010101 ± 0.13%	0.06466 ± 0.17%	63.6 ± 0.2	0.85	0.04643 ± 0.09%	19.8 ± 4.4
Sample 6. (MC-06-97) (Fig. 6g, h). Deformed leucogranite layer in domain 3, roadcut on Highway 23, 1.6 km south of Mica Creek Village at 580 m, 392580E-5761100N												
A	149	10	1516	27	5454	3	3.2	0.019273 ± 0.14%	0.12906 ± 0.16%	123.3 ± 0.4	0.83	0.04857 ± 0.09%	127.1 ± 4.3
B	149	6	1801	32	3662	4	3.5	0.019100 ± 0.17%	0.12762 ± 0.21%	122.0 ± 0.5	0.86	0.04846 ± 0.11%	121.9 ± 5.0
C	149	5	2888	51	5209	3	3.4	0.019000 ± 0.10%	0.12710 ± 0.15%	121.5 ± 0.3	0.74	0.04852 ± 0.10%	124.5 ± 4.9
1	149	19	6700	464	5164	24	79.8	0.015439 ± 0.13%	0.10177 ± 0.14%	98.4 ± 0.3	0.93	0.04781 ± 0.05%	89.7 ± 2.5
2	149	17	8286	324	6946	20	64.5	0.015311 ± 0.11%	0.10076 ± 0.12%	97.5 ± 0.2	0.94	0.04773 ± 0.04%	85.8 ± 2.0
3	149	14	7577	321	4298	24	67.7	0.015101 ± 0.13%	0.09873 ± 0.16%	95.6 ± 0.3	0.81	0.04742 ± 0.09%	70.4 ± 4.5
4	105	13	8338	325	4454	24	64.6	0.015250 ± 0.11%	0.09954 ± 0.12%	96.3 ± 0.2	0.91	0.04734 ± 0.05%	66.3 ± 2.5
5	105	7	10320	718	4748	15	65.7	0.015041 ± 0.09%	0.09948 ± 0.11%	96.3 ± 0.2	0.89	0.04797 ± 0.05%	97.7 ± 2.5
X1	149	10	11566	158	9114	12	5.0	0.014374 ± 0.14%	0.09497 ± 0.15%	92.1 ± 0.3	0.97	0.04792 ± 0.04%	95.2 ± 1.7
Sample 7. (MC-07-97) (Fig. 6f). Undeformed pegmatite dyke in domain 3, roadcut on Highway 23, 1.3 km south of Mica Creek Village at 580 m, 392580E-5761340N												
1	105	6	53042	741	3936	52	35.1	0.010056 ± 0.13%	0.06379 ± 0.15%	62.8 ± 0.2	0.90	0.04601 ± 0.06%	-1.9 ± 3.1
2	105	4	43541	615	3454	32	36.6	0.009918 ± 0.14%	0.06345 ± 0.15%	62.5 ± 0.2	0.87	0.04639 ± 0.08%	18.1 ± 3.6
3	105	5	26218	351	3520	23	34.2	0.009766 ± 0.13%	0.06353 ± 0.15%	62.5 ± 0.2	0.91	0.04718 ± 0.06%	58.1 ± 3.0
4	105	5	32334	472	3516	29	38.2	0.009996 ± 0.12%	0.06388 ± 0.15%	62.9 ± 0.2	0.91	0.04635 ± 0.06%	15.7 ± 3.0
Sample 26. (MC-26-98) (Fig. 4d). Migmatitic kyanite schist in domain 3, roadcut on Highway 23, 1.7 km south of Mica Creek Village at 580 m, 392560E-5761000N												
1	149	11	9494	443	4282	23	71.5	0.014645 ± 0.11%	0.09600 ± 0.12%	93.1 ± 0.2	0.93	0.04754 ± 0.05%	76.5 ± 2.3
2	149	8	14325	558	4909	23	64.9	0.015110 ± 0.12%	0.09942 ± 0.14%	96.2 ± 0.3	0.92	0.04772 ± 0.05%	85.4 ± 2.5
3	149	5	17970	993	2948	34	71.3	0.017487 ± 0.12%	0.11607 ± 0.13%	111.5 ± 0.3	0.72	0.04814 ± 0.10%	106.2 ± 4.5
4	149	6	12807	604	4315	17	71.4	0.014855 ± 0.12%	0.09727 ± 0.12%	94.3 ± 0.2	0.78	0.04749 ± 0.08%	73.8 ± 3.7
5	149	9	9965	370	3883	22	64.0	0.014731 ± 0.11%	0.09730 ± 0.13%	94.3 ± 0.2	0.91	0.04790 ± 0.05%	94.4 ± 2.5
6	149	6	20218	802	3557	38	60.7	0.017192 ± 0.11%	0.11554 ± 0.13%	111.0 ± 0.3	0.92	0.04874 ± 0.05%	135.5 ± 2.5
7	149	6	14433	607	2891	29	67.0	0.015328 ± 0.11%	0.10154 ± 0.13%	98.2 ± 0.2	0.85	0.04804 ± 0.07%	101.4 ± 3.3
8	149	8	12976	605	2957	35	69.7	0.015580 ± 0.12%	0.10362 ± 0.15%	100.1 ± 0.3	0.90	0.04824 ± 0.06%	110.8 ± 3.0

Table 1. (*continued*).

Analysis[a]	Weight[b] (μg)	U (ppm)	Pb*[c] (ppm)	$^{206}Pb/^{204}Pb$[d]	Pb_c[e] (pg)	^{208}Pb (%)[f]	$^{206}Pb/^{238}U$[g]	$^{207}Pb/^{235}U$[g]	$^{207}Pb/^{235}U$ age[h] (Ma)	Correlation coefficient	$^{207}Pb/^{206}Pb$[g]	$^{207}Pb/^{206}Pb$ age[h] (Ma)
Sample 28. (MC-28-98) (Fig. 4e). Migmatitic kyanite schist in domain 3; roadcut in Soards Creek valley at 1020 m, 389760E-57766260N												
1	202	21	8470	369	5252	33	68.6	0.015119 ± 0.12%	0.09869 ± 0.13%	95.6 ± 0.2	0.89	0.04734 ± 0.06%	66.5 ± 2.9
2	202	13	15821	674	6400	36	62.8	0.017478 ± 0.17%	0.11509 ± 0.15%	110.6 ± 0.3	0.80	0.04776 ± 0.10%	87.3 ± 5.0
3	202	25	13424	309	5395	43	58.0	0.010686 ± 0.14%	0.06869 ± 0.15%	67.5 ± 0.2	0.95	0.04662 ± 0.05%	29.9 ± 2.3
4	149	13	10645	388	4621	26	66.2	0.013611 ± 0.10%	0.08998 ± 0.14%	87.5 ± 0.2	0.82	0.04795 ± 0.08%	96.6 ± 3.8
5	149	10	19803	920	6766	35	63.9	0.018508 ± 0.14%	0.12420 ± 0.15%	118.9 ± 0.3	0.90	0.04867 ± 0.06%	131.9 ± 3.0
6	149	9	12230	612	4864	25	69.2	0.017015 ± 0.11%	0.11302 ± 0.13%	108.7 ± 0.3	0.93	0.04818 ± 0.05%	108.0 ± 2.2
Sample 29. (MC-29-98) (Fig. 4g). Migmatitic staurolite-sillimanite schist in domain 3; roadcut in Soards Creek valley at 1030 m, 382900E-5766340N												
1	149	7	8113	345	2826	20	66.4	0.015775 ± 0.10%	0.10429 ± 0.14%	100.7 ± 0.3	0.74	0.04795 ± 0.10%	96.6 ± 4.5
2	105	4	11239	428	2492	18	63.5	0.015348 ± 0.14%	0.10131 ± 0.16%	98.0 ± 0.3	0.83	0.04787 ± 0.09%	93.1 ± 4.3
3	149	10	7218	295	2830	25	66.6	0.015055 ± 0.11%	0.09956 ± 0.13%	96.4 ± 0.2	0.87	0.04796 ± 0.07%	97.4 ± 3.1
4	105	6	9301	410	2371	22	69.8	0.014690 ± 0.11%	0.09698 ± 0.14%	94.0 ± 0.2	0.81	0.04788 ± 0.08%	93.4 ± 3.8
5	105	4	10954	580	3481	15	67.8	0.018801 ± 0.09%	0.12596 ± 0.12%	120.5 ± 0.3	0.90	0.04859 ± 0.05%	128.1 ± 2.6

Notes: Isotopic composition of Carleton University laboratory blank (uncertainty is 1σ): 206:207:208:204 = 19.01 ± 0.36 : 15.64 ± 0.20 : 38.23 ± 0.74 : 1; UTM coordinates in grid zone 11. [a]A-E in first column, fraction codes for zircon analyses; 1-8, fraction codes for monazite analyses; X1-X3, fraction code for xenotime analysis; 105-202, average size in μm. [b]Weights were estimated from grain size measurements; uncertainty is 2 μg. [c]Radiogenic Pb. [d]Measured ratio, corrected for spike and Pb fractionation of 0.09 ± 0.03%/a.m.u. [e]Total common Pb in analysis, corrected for spike and fractionation. [f]Radiogenic ^{208}Pb, expressed as percentage of total radiogenic Pb. [g]Corrected for blank Pb and U and common Pb (Stacey-Kramers model Pb composition equivalent to the interpreted age of the analyses); errors are 1σ in percent. [h]Errors are 2σ in Ma.

Table 2. U-Th-Pb SHRIMP analytical data.

Spot[a]	U (ppm)	Th (ppm)	Th/U	Pb* (ppm)	^{204}Pb (ppb)	^{206}Pb/^{204}Pb	^{208}Pb[b]/^{232}Th	^{206}Pb[b]/^{238}U	^{207}Pb[b]/^{235}U	^{207}Pb[b]/^{206}Pb	^{208}Pb[c]/^{232}Th age (Ma)	^{206}Pb[c]/^{238}U age (Ma)	^{207}Pb[c]/^{235}U age (Ma)
Sample 9. (MC-09-97) (Fig. 5a). Garnet schist in domain 1; head of Franchère Creek at 2200 m, 392540E-5785600N													
M-1.1	4429	17245	3.9	221	34	2256	0.00723 ± 0.00021	0.02366 ± 0.00055	0.1518 ± 0.0058	0.0465 ± 0.0013	145.6 ± 4.2	150.8 ± 3.5	143.5 ± 5.1
M-1.2	3547	15820	4.5	188	20	4847	0.00748 ± 0.00018	0.02459 ± 0.00032	0.1619 ± 0.0041	0.0477 ± 0.0010	150.6 ± 3.6	156.6 ± 2.0	152.3 ± 3.6
M-1.3	3113	13066	4.2	63	16	1564	0.00302 ± 0.00009	0.00893 ± 0.00014	0.0535 ± 0.0052	0.0434 ± 0.0041	61.0 ± 1.9	57.3 ± 0.9	52.9 ± 5.0
M-2.1	4302	29074	6.8	308	26	3546	0.00770 ± 0.00011	0.02416 ± 0.00054	0.1552 ± 0.0076	0.0466 ± 0.0019	155.0 ± 2.2	153.9 ± 3.4	146.5 ± 6.7
M-2.2	2859	35359	12.4	306	31	1950	0.00726 ± 0.00010	0.02363 ± 0.00026	0.1469 ± 0.0053	0.0451 ± 0.0015	146.3 ± 1.9	150.5 ± 1.7	139.2 ± 4.7
M-3.1	3645	26254	7.2	104	32	1213	0.00306 ± 0.00007	0.00901 ± 0.00014	0.0594 ± 0.0047	0.0478 ± 0.0036	61.7 ± 1.5	57.8 ± 0.9	58.6 ± 4.5
M-4.1	2677	20613	7.7	92	76	240	0.00296 ± 0.00011	0.00969 ± 0.00016	0.0559 ± 0.0110	0.0418 ± 0.0081	59.8 ± 2.2	62.2 ± 1.0	55.2 ± 10.6
M-5.1	5141	39882	7.8	445	20	5260	0.00857 ± 0.00015	0.02476 ± 0.00029	0.1676 ± 0.0043	0.0491 ± 0.0011	172.5 ± 3.0	157.7 ± 1.8	157.4 ± 3.8
M-5.2	3374	32366	9.6	315	12	4108	0.00717 ± 0.00024	0.02340 ± 0.00035	0.1492 ± 0.0049	0.0462 ± 0.0013	144.3 ± 4.8	149.1 ± 2.2	141.2 ± 4.3
M-6.1	2821	23036	8.2	238	22	3453	0.00821 ± 0.00009	0.02497 ± 0.00023	0.1677 ± 0.0054	0.0487 ± 0.0014	165.3 ± 1.8	159.0 ± 1.4	157.4 ± 4.7
M-6.2	3070	25286	8.2	255	19	4077	0.00792 ± 0.00008	0.02492 ± 0.00022	0.1624 ± 0.0045	0.0473 ± 0.0012	159.4 ± 1.6	158.7 ± 1.4	152.8 ± 4.0
M-6.3	3747	25613	6.8	109	14	1966	0.00309 ± 0.00005	0.00938 ± 0.00010	0.0582 ± 0.0063	0.0450 ± 0.0048	62.3 ± 1.1	60.2 ± 0.7	57.4 ± 6.0
M-6.4	3433	28290	8.2	283	17	4337	0.00763 ± 0.00015	0.02500 ± 0.00036	0.1630 ± 0.0054	0.0473 ± 0.0013	153.6 ± 3.1	159.2 ± 2.3	153.3 ± 4.8
M-6.5	4564	39365	8.6	151	41	950	0.00289 ± 0.00009	0.00976 ± 0.00017	0.0580 ± 0.0039	0.0431 ± 0.0027	58.4 ± 1.7	62.6 ± 1.1	57.3 ± 3.8
M-6.6	4476	31029	6.9	124	32	1237	0.00285 ± 0.00004	0.00956 ± 0.00010	0.0548 ± 0.0038	0.0416 ± 0.0028	57.6 ± 0.8	61.3 ± 0.6	54.1 ± 3.7
M-8.1	2517	9982	4.0	49	5	3029	0.00280 ± 0.00004	0.00862 ± 0.00010	0.0547 ± 0.0054	0.0460 ± 0.0045	56.5 ± 0.8	55.3 ± 0.6	54.1 ± 5.2
M-8.2	4058	15942	3.9	79	42	726	0.00277 ± 0.00012	0.00917 ± 0.00026	0.0497 ± 0.0042	0.0393 ± 0.0030	55.9 ± 2.5	58.8 ± 1.7	49.3 ± 4.1
G-1.1	1418	9006	6.4	132	60	308	0.00800 ± 0.00013	0.02879 ± 0.00071	0.1805 ± 0.0284	0.0455 ± 0.0070	161.1 ± 2.7	183.0 ± 4.4	168.5 ± 24.8
Sample 1. (MC-01-97) (Fig. 5b). Migmatitic kyanite schist in domain 2; roadcut on Highway 23, 0.5 km south of Mica Dam at 740 m, 393180E-5770260N													
G-1.1	2456	30938	12.6	194	55	916	0.00560 ± 0.00010	0.01805 ± 0.00031	0.1162 ± 0.0078	0.0467 ± 0.0029	112.8 ± 1.9	115.3 ± 2.0	111.7 ± 7.1
G-1.2	2869	46499	16.2	275	52	965	0.00541 ± 0.00010	0.01827 ± 0.00033	0.1287 ± 0.0097	0.0511 ± 0.0036	109.0 ± 2.0	116.7 ± 2.1	122.9 ± 8.8
G-1.3	2680	46444	17.3	273	56	803	0.00544 ± 0.00010	0.01783 ± 0.00032	0.1221 ± 0.0096	0.0497 ± 0.0037	109.7 ± 2.0	113.9 ± 2.0	116.0 ± 8.7
K-1.1	3965	29267	7.4	146	96	486	0.00378 ± 0.00007	0.01187 ± 0.00020	0.0747 ± 0.0051	0.0457 ± 0.0029	76.2 ± 1.4	76.1 ± 1.3	73.2 ± 4.8
K-1.2	5619	37242	6.6	194	114	543	0.00376 ± 0.00007	0.01204 ± 0.00021	0.0698 ± 0.0076	0.0421 ± 0.0044	75.8 ± 1.4	77.1 ± 1.4	68.5 ± 7.3
K-1.3	5959	35423	5.9	186	173	390	0.00362 ± 0.00006	0.01160 ± 0.00020	0.0750 ± 0.0058	0.0469 ± 0.0034	73.0 ± 1.3	74.3 ± 1.3	73.4 ± 5.5
K-2.1	4746	36253	7.6	193	114	539	0.00412 ± 0.00007	0.01274 ± 0.00022	0.0811 ± 0.0043	0.0462 ± 0.0022	83.2 ± 1.4	81.6 ± 1.4	79.1 ± 4.0
K-2.2	4440	32219	7.3	166	65	848	0.00393 ± 0.00007	0.01255 ± 0.00021	0.0806 ± 0.0038	0.0466 ± 0.0019	79.3 ± 1.4	80.4 ± 1.3	78.7 ± 3.5
K-3.1	5743	39160	6.8	210	78	970	0.00405 ± 0.00008	0.01273 ± 0.00021	0.0855 ± 0.0036	0.0487 ± 0.0018	81.7 ± 1.6	81.5 ± 1.4	83.3 ± 3.4
K-4.1	5753	41633	7.2	220	83	905	0.00405 ± 0.00007	0.01285 ± 0.00022	0.0824 ± 0.0053	0.0465 ± 0.0028	81.7 ± 1.4	82.3 ± 1.4	80.4 ± 4.9
K-5.1	5635	32192	5.7	177	95	756	0.00391 ± 0.00007	0.01201 ± 0.00020	0.0766 ± 0.0035	0.0463 ± 0.0019	78.8 ± 1.3	77.0 ± 1.3	75.0 ± 3.3
K-5.2	5725	32555	5.7	182	74	921	0.00390 ± 0.00007	0.01241 ± 0.00021	0.0790 ± 0.0044	0.0462 ± 0.0024	78.7 ± 1.4	79.5 ± 1.4	77.2 ± 4.2
M-1.1	7159	34988	4.9	194	173	537	0.00365 ± 0.00006	0.01143 ± 0.00019	0.0731 ± 0.0032	0.0464 ± 0.0018	73.7 ± 1.3	73.3 ± 1.2	71.6 ± 3.0
M-1.2	6438	36216	5.6	171	139	442	0.00319 ± 0.00006	0.01018 ± 0.00017	0.0612 ± 0.0043	0.0436 ± 0.0029	64.3 ± 1.2	65.3 ± 1.1	60.3 ± 4.1
M-1.3	5175	25544	4.9	157	53	1244	0.00410 ± 0.00007	0.01307 ± 0.00022	0.0841 ± 0.0033	0.0467 ± 0.0016	82.7 ± 1.4	83.7 ± 1.4	82.0 ± 3.1
M-1.4	8218	40521	4.9	243	92	898	0.00384 ± 0.00007	0.01267 ± 0.00021	0.0857 ± 0.0032	0.0491 ± 0.0016	77.6 ± 1.4	81.1 ± 1.4	83.5 ± 3.0
M-1.5	11120	43271	3.9	230	110	740	0.00302 ± 0.00005	0.00995 ± 0.00016	0.0637 ± 0.0027	0.0464 ± 0.0017	61.0 ± 1.1	63.8 ± 1.1	62.7 ± 2.6

Table 2. (*continued*).

Spot[a]	U (ppm)	Th (ppm)	Th/U	Pb* (ppm)	^{204}Pb (ppb)	^{206}Pb/^{204}Pb	^{208}Pb/^{232}Th[b]	^{206}Pb/^{238}U[b]	^{207}Pb/^{235}U[b]	^{207}Pb/^{206}Pb[b]	^{208}Pb/^{232}Th age (Ma)[c]	^{206}Pb/^{238}U age (Ma)[c]	^{207}Pb/^{235}U age (Ma)[c]
M-2.1	9067	37851	4.2	247	91	1189	0.00405 ± 0.00007	0.01283 ± 0.00021	0.0843 ± 0.0029	0.0476 ± 0.0014	81.6 ± 1.5	82.2 ± 1.3	82.1 ± 2.8
M-2.2	7225	33051	4.6	206	92	854	0.00392 ± 0.00007	0.01267 ± 0.00022	0.0857 ± 0.0034	0.0491 ± 0.0016	79.1 ± 1.5	81.2 ± 1.4	83.5 ± 3.2
M-2.3	12421	41504	3.3	315	213	732	0.00416 ± 0.00007	0.01330 ± 0.00022	0.0905 ± 0.0036	0.0494 ± 0.0017	84.0 ± 1.5	85.2 ± 1.4	88.0 ± 3.3
M-3.1	5379	41731	7.8	220	78	832	0.00410 ± 0.00007	0.01279 ± 0.00021	0.0890 ± 0.0037	0.0505 ± 0.0018	82.8 ± 1.4	81.9 ± 1.4	86.5 ± 3.4

Notes: [a] Spots are denoted as follows: G = monazite inclusion in garnet, K = monazite inclusion in kyanite, M = matrix monazite. [b]Errors are 1 σ. [c]Errors are 1σ in Ma.

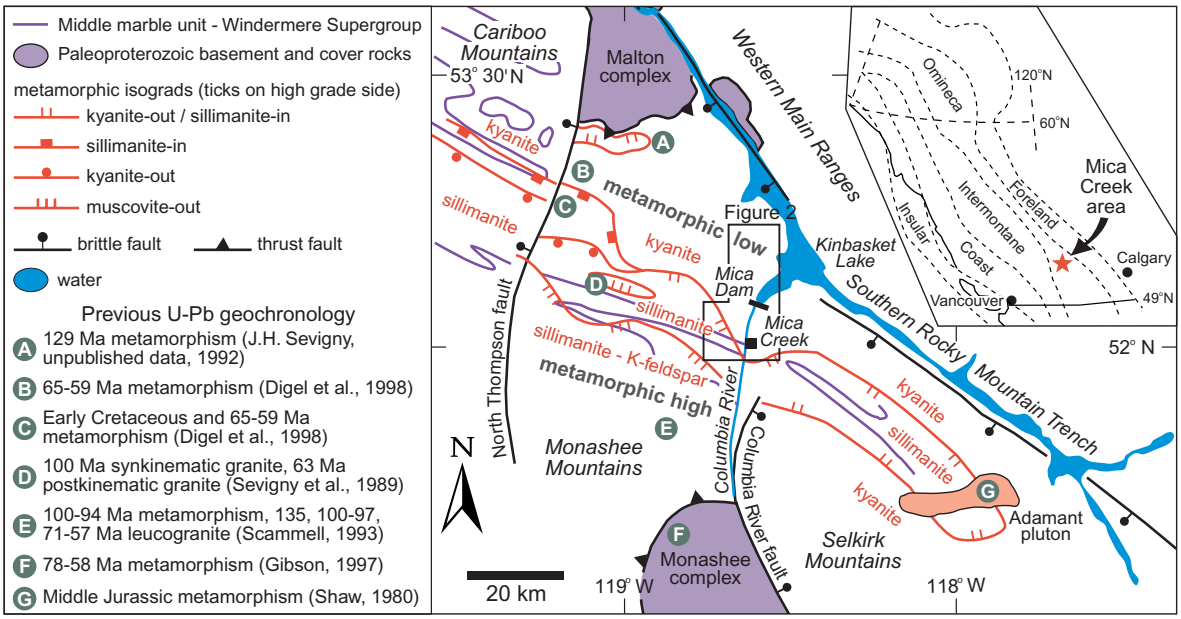

Figure 1. Regional geologic map showing the location of the Mica Creek area relative to the metamorphic isograds and previous U-Pb localities in the Selkirk-Monashee-Cariboo complex. The inset map locates the Mica Creek area with respect to the morphogeologic belts of the Canadian Cordillera.

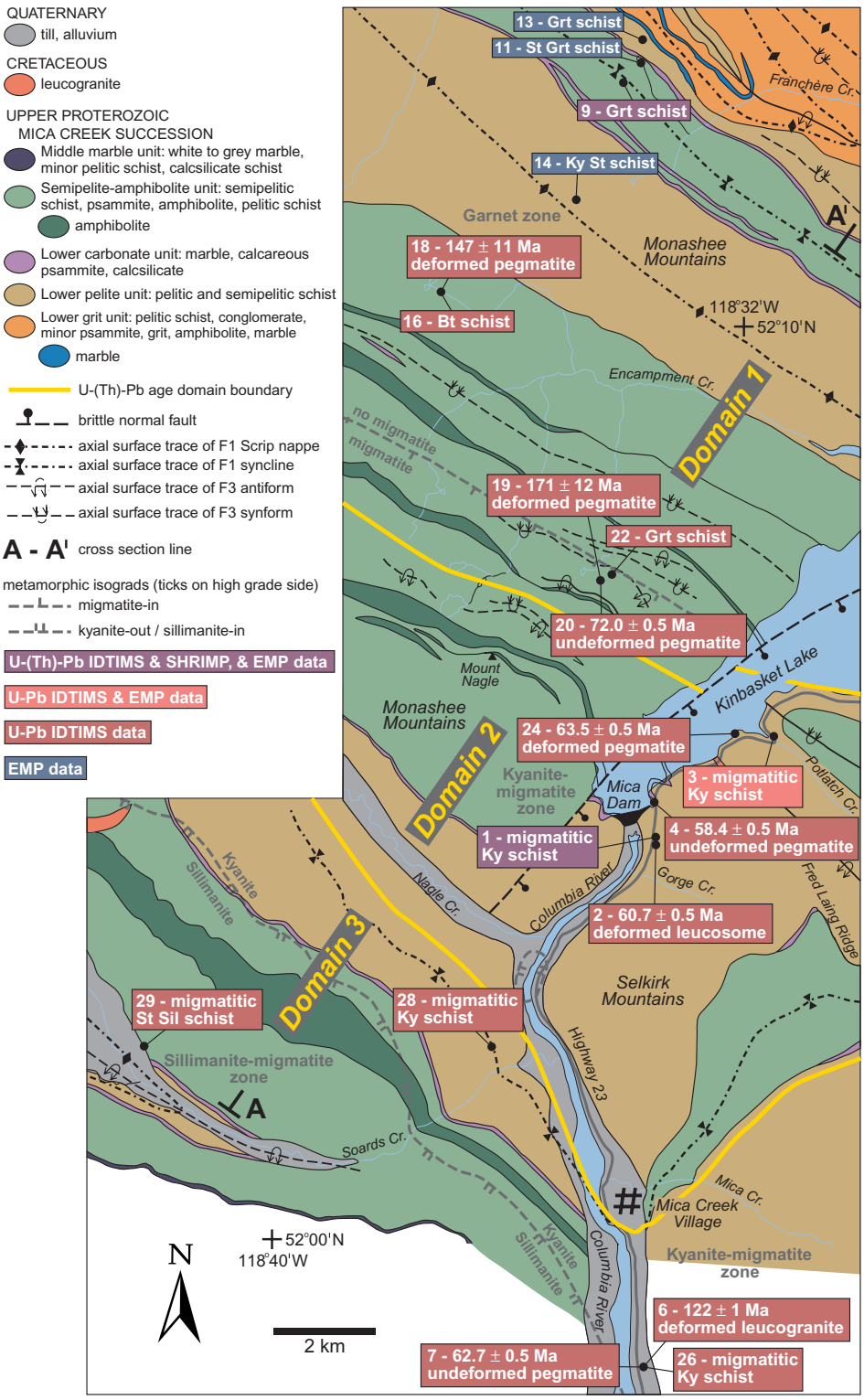

Figure 2. Geologic map of the Mica Creek area (after McDonough et al. (1992)) showing the location of samples. U-Pb ages are shown for the granitoid rocks. Line A-A locates the cross section in Fig. 3. Mineral abbreviations after Kretz (1983).

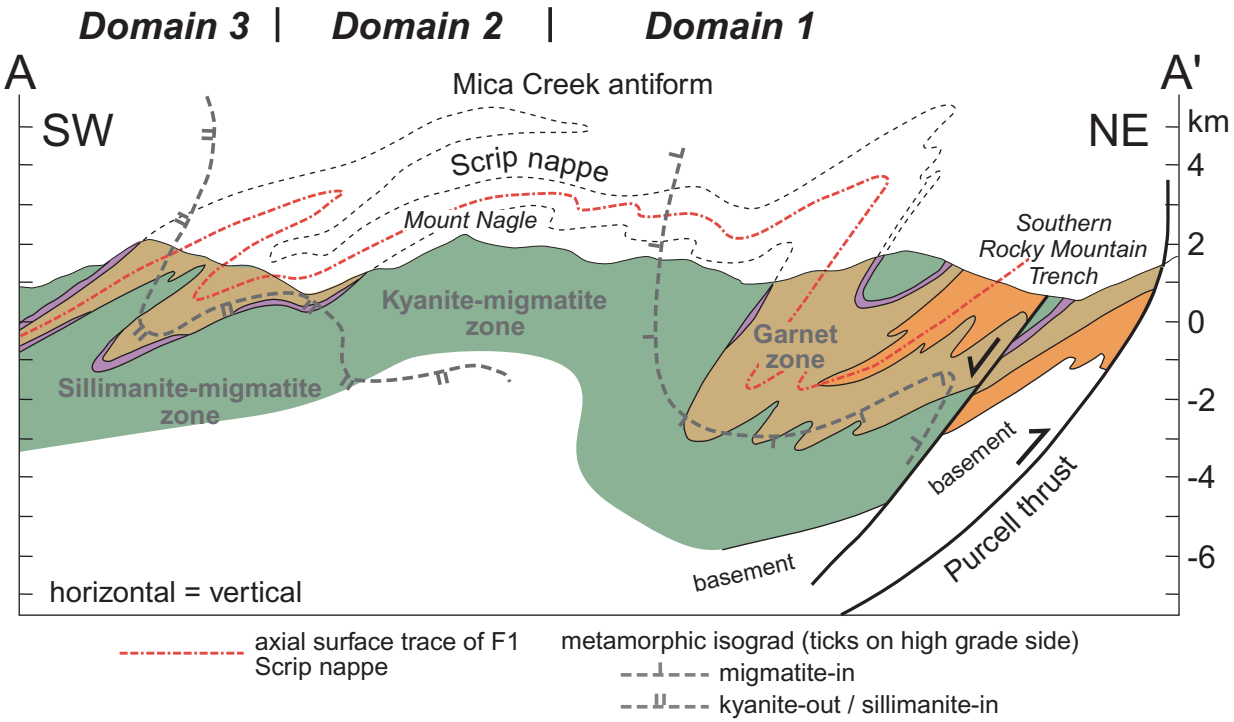

Figure 3. Cross section of the Mica Creek area (after Simony et al. (1980)) illustrating the apparent metamorphic and structural continuity across the area. Location of the section, patterns for rock units, and symbols are shown in Fig. 2.

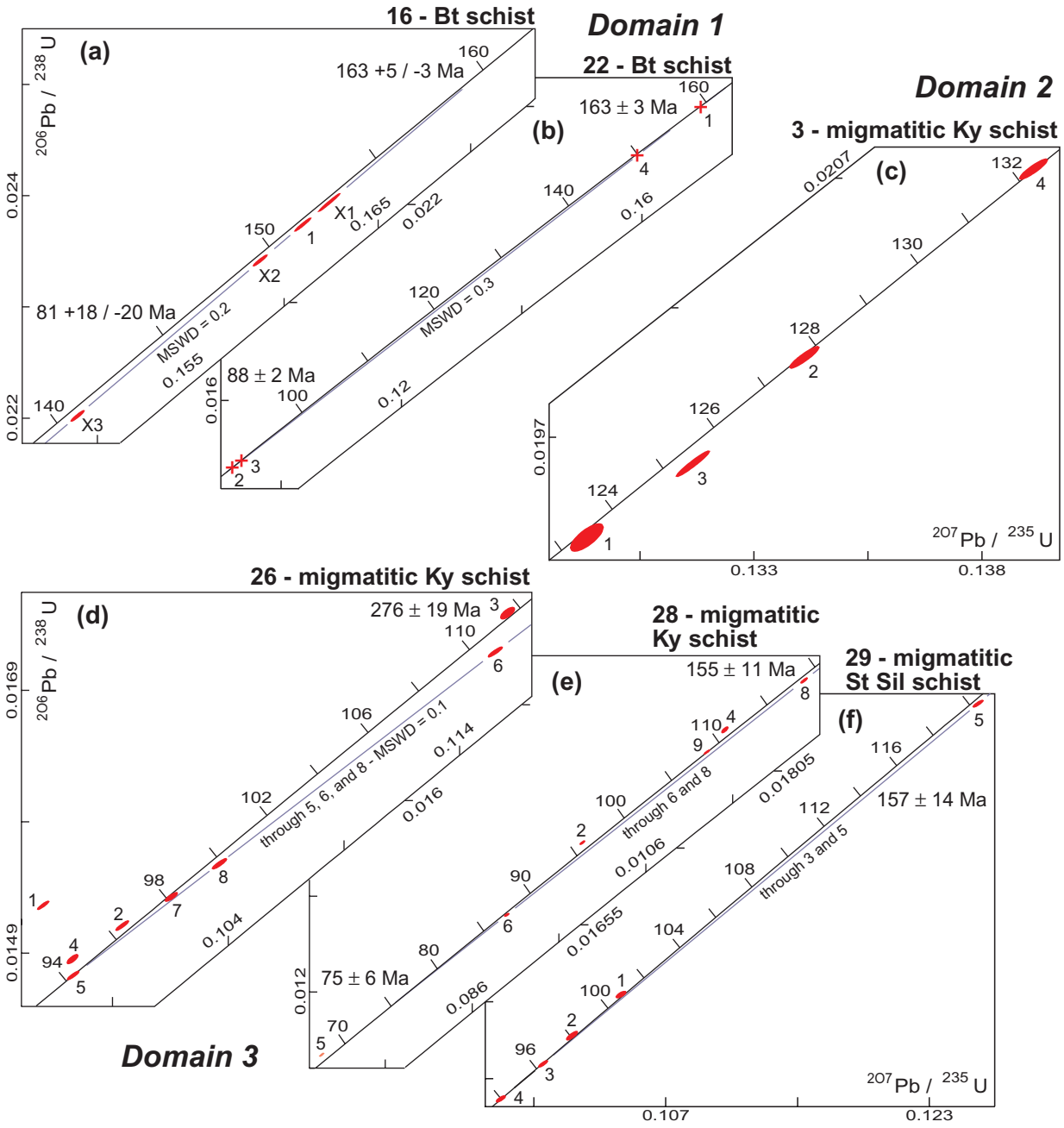

Figure 4. U-Pb concordia plots for schists, except for samples 1 and 9. Ellipses for the analyses represent the 2σ uncertainty and analyses that are plotted with + symbols have ellipses that are too small to be seen at this scale. Monazite analyses are identified with numbers and xenotime analyses are identified with X1-X3. See Table 1 for analytical data. Mineral abbreviations after Kretz (1983).

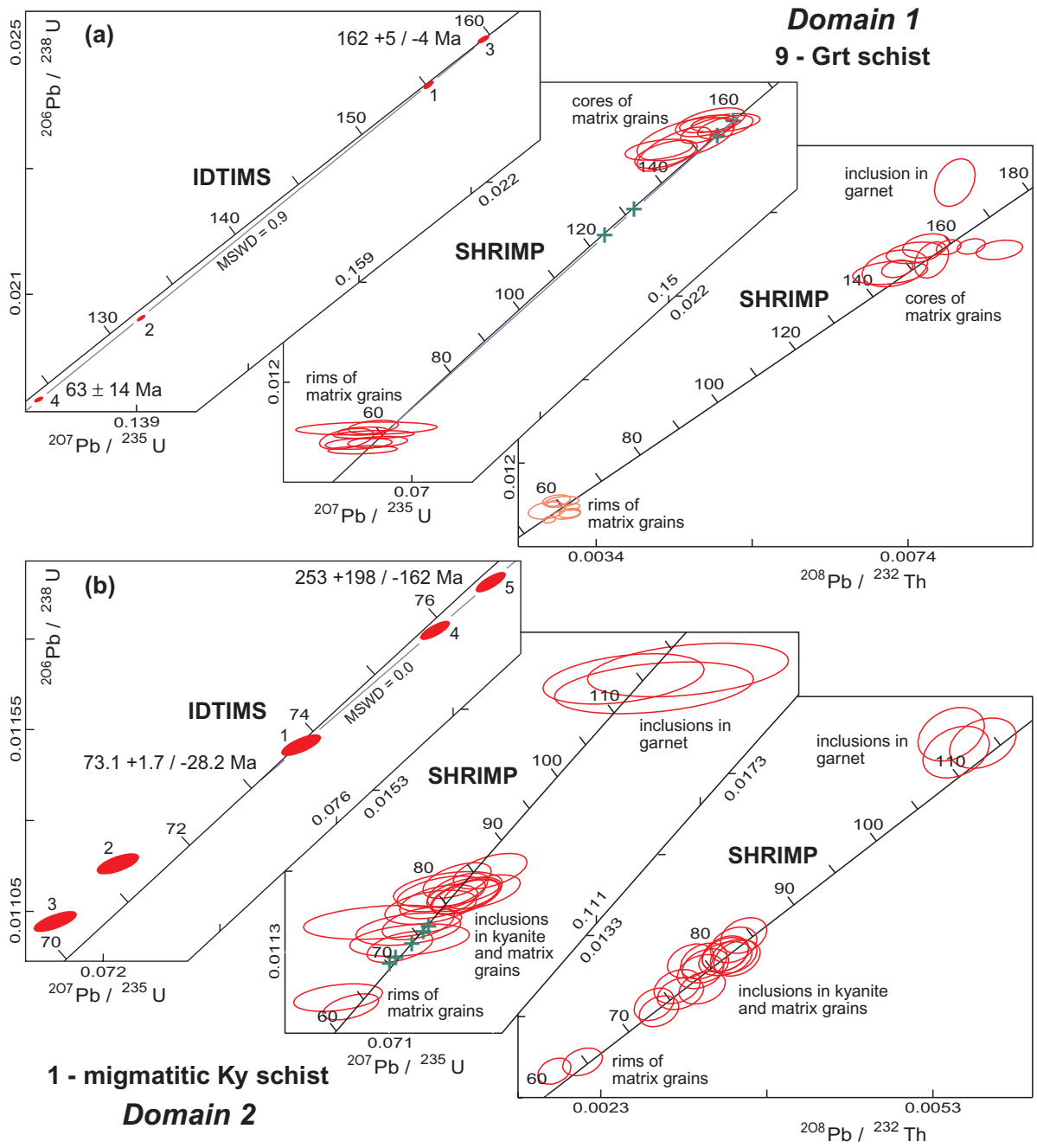

Figure 5. U-Pb concordia plots of IDTIMS data and U-Th-Pb concordia plots of SHRIMP data from samples 1 and 9. Ellipses for the analyses represent the 2σ uncertainty. IDTIMS analyses are shown on the U-Pb SHRIMP plots by + symbols that are significantly larger than the 2σ uncertainty. Monazite analyses are identified with numbers and zircon analyses are identified with letters. See Tables 1 and 2 for analytical data. Mineral abbreviations after Kretz (1983).

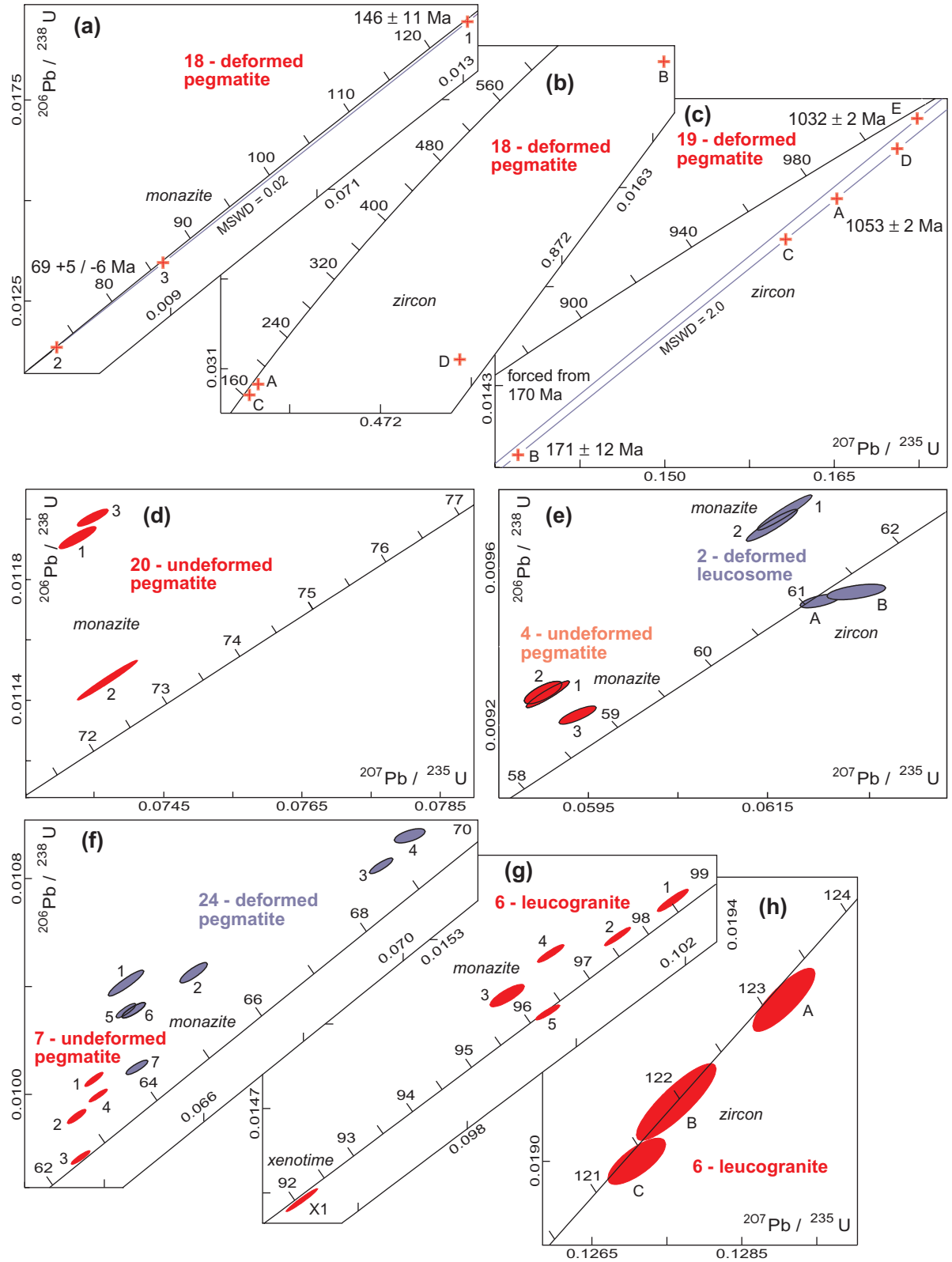

Figure 6. U-Pb concordia plots for granitoid rocks. Ellipses for the analyses represent the 2σ uncertainty and analyses that are plotted with + symbols have ellipses that are too small to be seen at this scale. Zircon analyses are identified with letters and monazite analyses are identified with numbers. See Table 1 for analytical data.

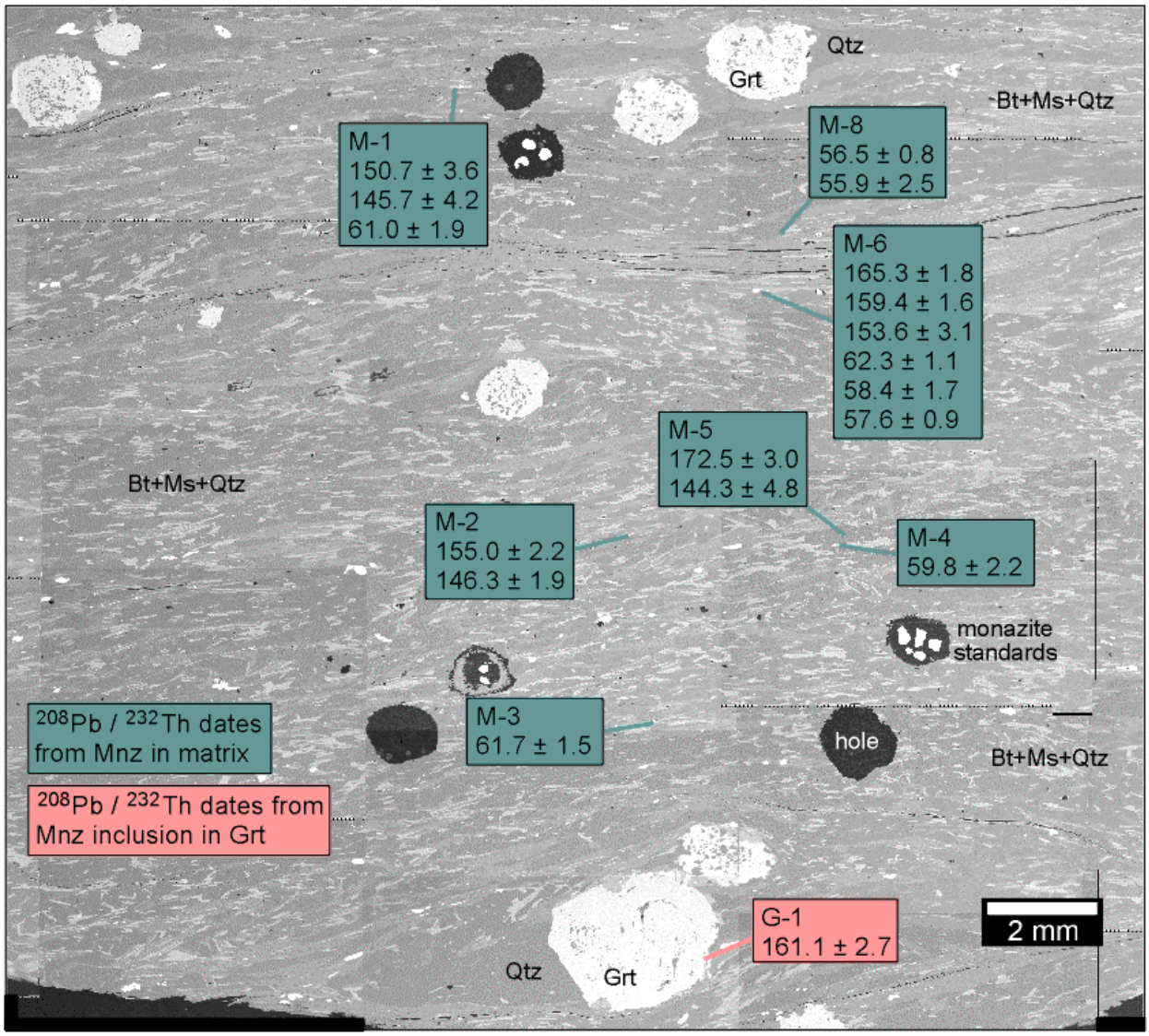

Figure 7. BSE image of a thin section from sample 9 showing the location of monazites dated with the SHRIMP and the $^{208}Pb/^{232}Th$ ages (1σ uncertainty). Mineral abbreviations after Kretz (1983).

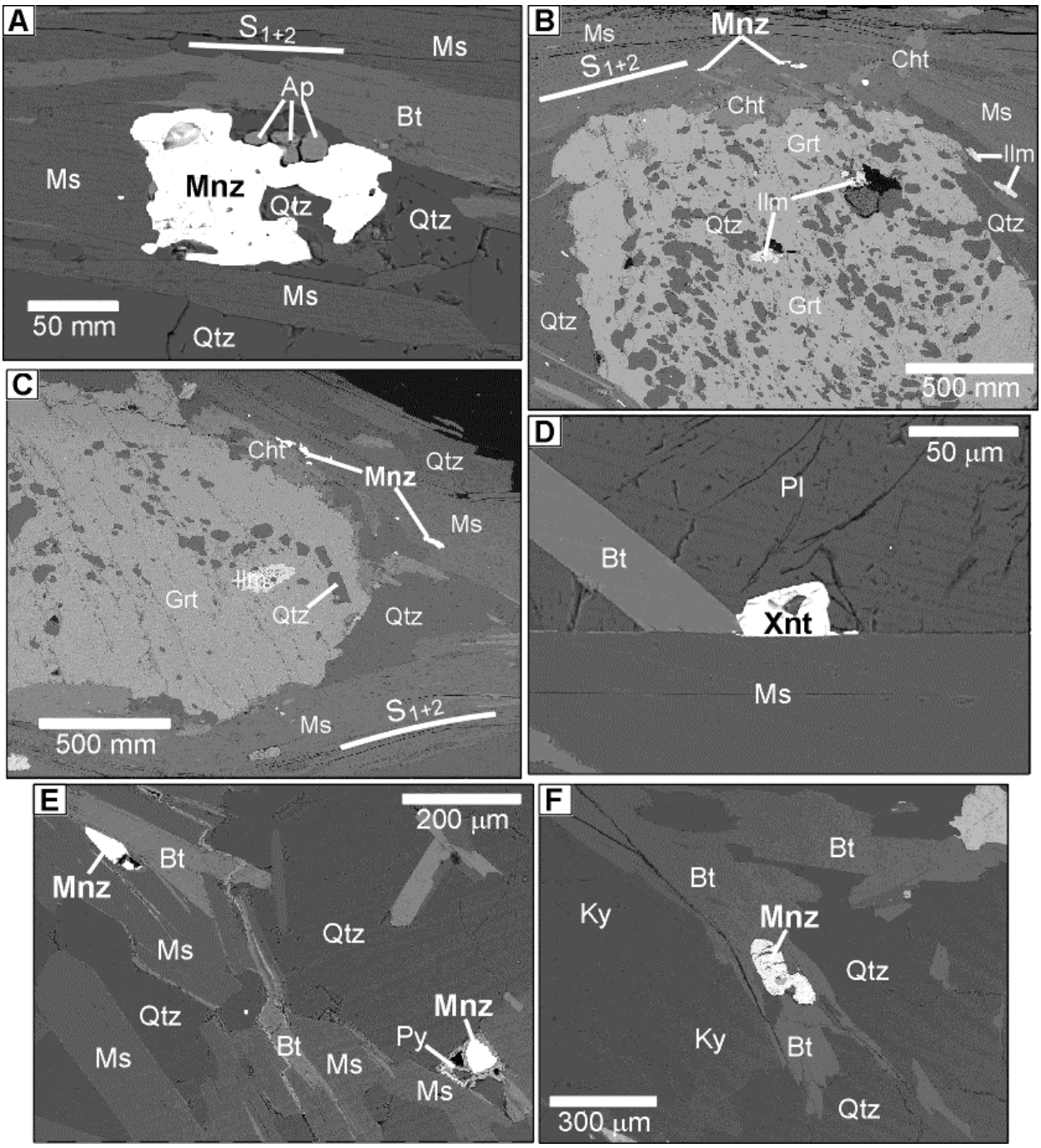

Figure 8. BSE images of monazite and xenotime (white grains) in thin section. (a) apatite in sample 9 exists within embayments into monazite. (b, c) monazite in sample 9 lies within S_{1+2} where it envelopes garnet. Note the quartz-filled pressure shadows around garnet and the foliation in garnet in (b) that was overgrown before final S_{1+2} development. (d) xenotime in sample 16 lies along biotite and muscovite grain boundaries. (e) monazite in sample 22 lies within S_{1+2} at muscovite and biotite grain boundaries. Some grains are associated with pyrite. (f) monazite in sample 3 lies within S_{1+2} at biotite and kyanite grain boundaries.

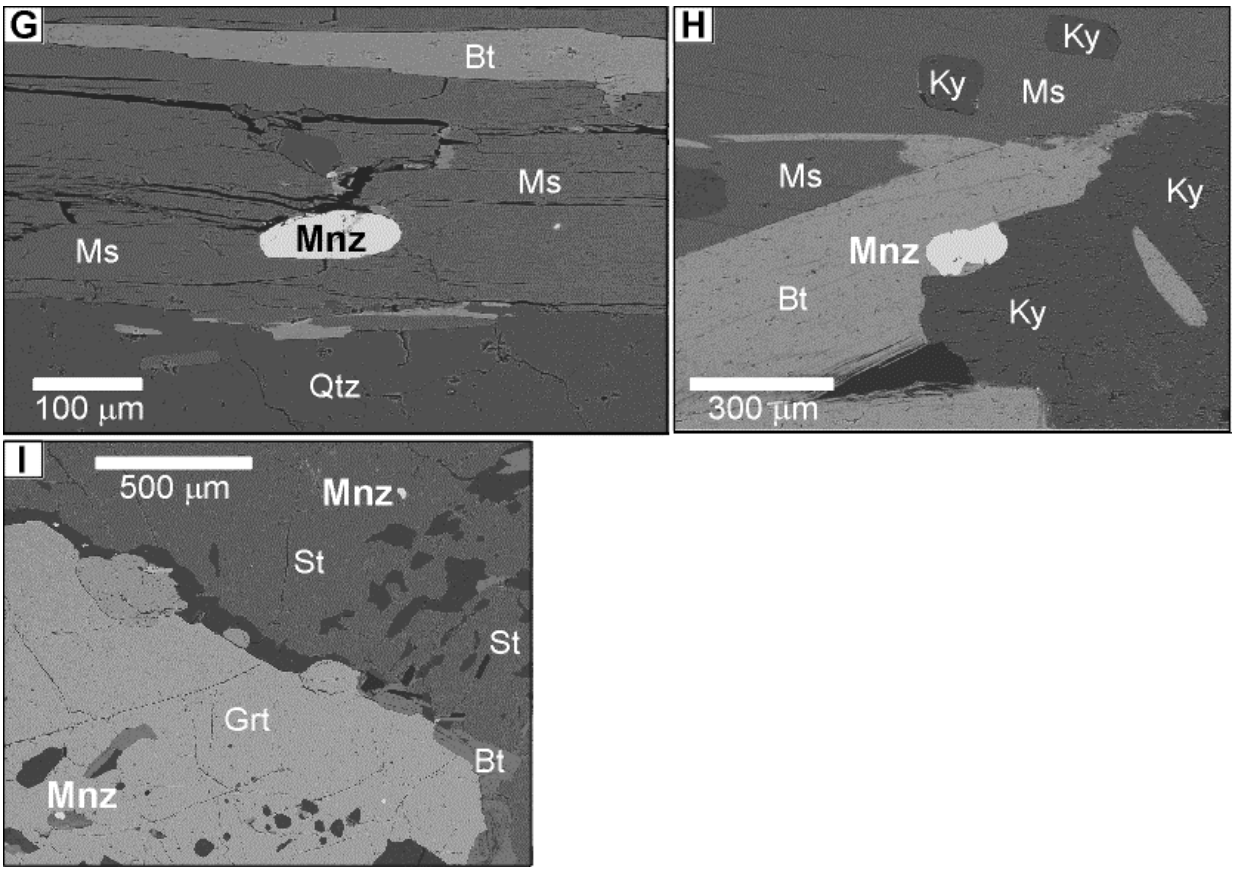

Figure 8 (*continued*). (g) monazite in sample 26 lies within S_{1+2} as inclusions in biotite. (h) monazite in sample 28 lies within S_{1+2} at biotite, muscovite, and kyanite grain boundaries. (i) monazite in sample 29 exists as inclusions in garnet and staurolite. Mineral abbreviations after Kretz (1983).

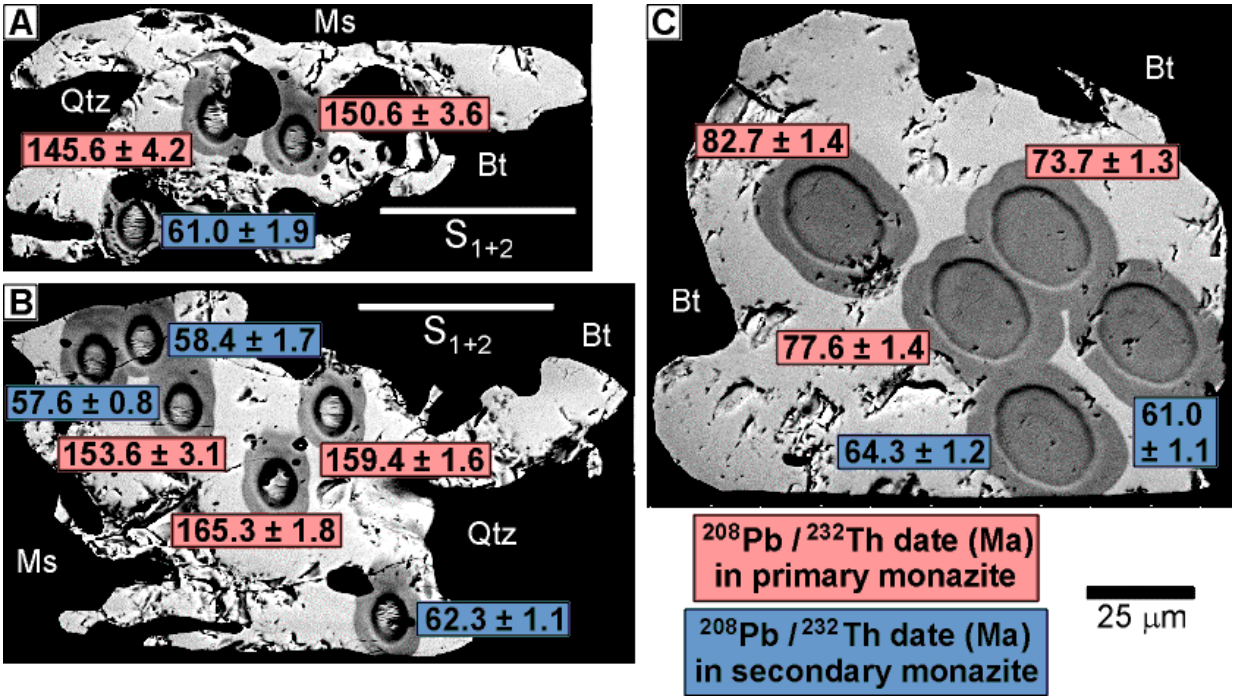

Figure 9. BSE images of selected monazites in thin section showing the location of the SHRIMP spots and $^{208}Pb/^{232}Th$ ages (1σ uncertainty). (a) sample 9, grain M-1. (b) sample 9, grain M-6. (c) sample 1, grain M-1. Mineral abbreviations after Kretz (1983).

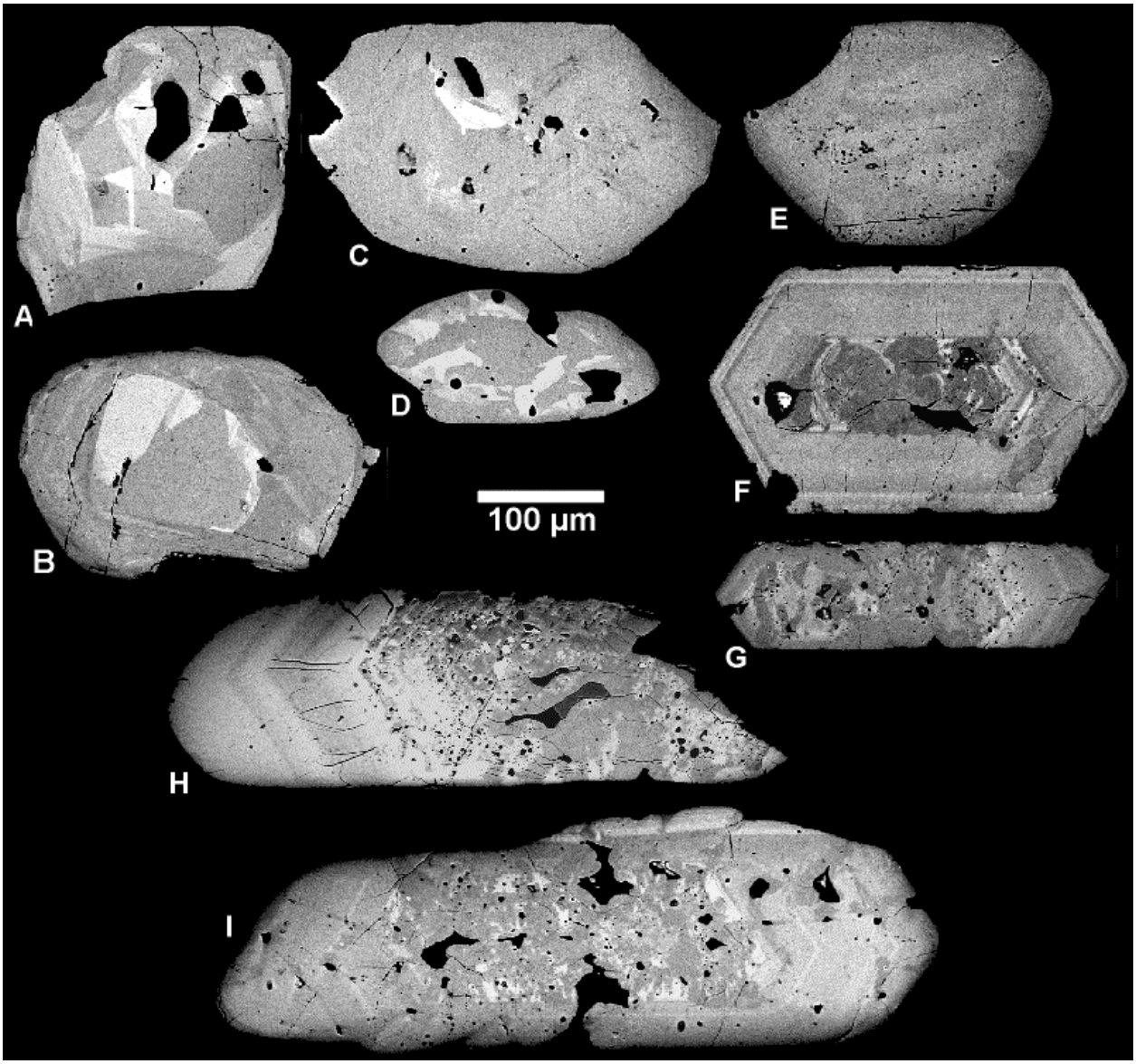

Figure 10. BSE images of polished grains show domains of varying brightness that correspond to differences in the average atomic number (mainly controlled by Th concentration in monazite and U and Y concentration in zircon and xenotime, respectively). (a, b) xenotime from sample 16 shows complex zoning patterns that indicate dissolution, recrystallization, and overgrowth. (c, d) monazite from sample 22 contains irregularly distributed Th-rich zones that indicate dissolution, recrystallization, and overgrowth. In (c), an oscillatory zoned core is surrounded along an irregular boundary by an unzoned rim. (e) monazite from sample 3 contains irregularly distributed, moderately Th-rich zones. (f, g) zircon from sample 18 contains altered cores with that are overgrown by oscillatory zoned rims. (h, i) zircon from sample 19 contains altered cores that are overgrown by oscillatory zoned rims.

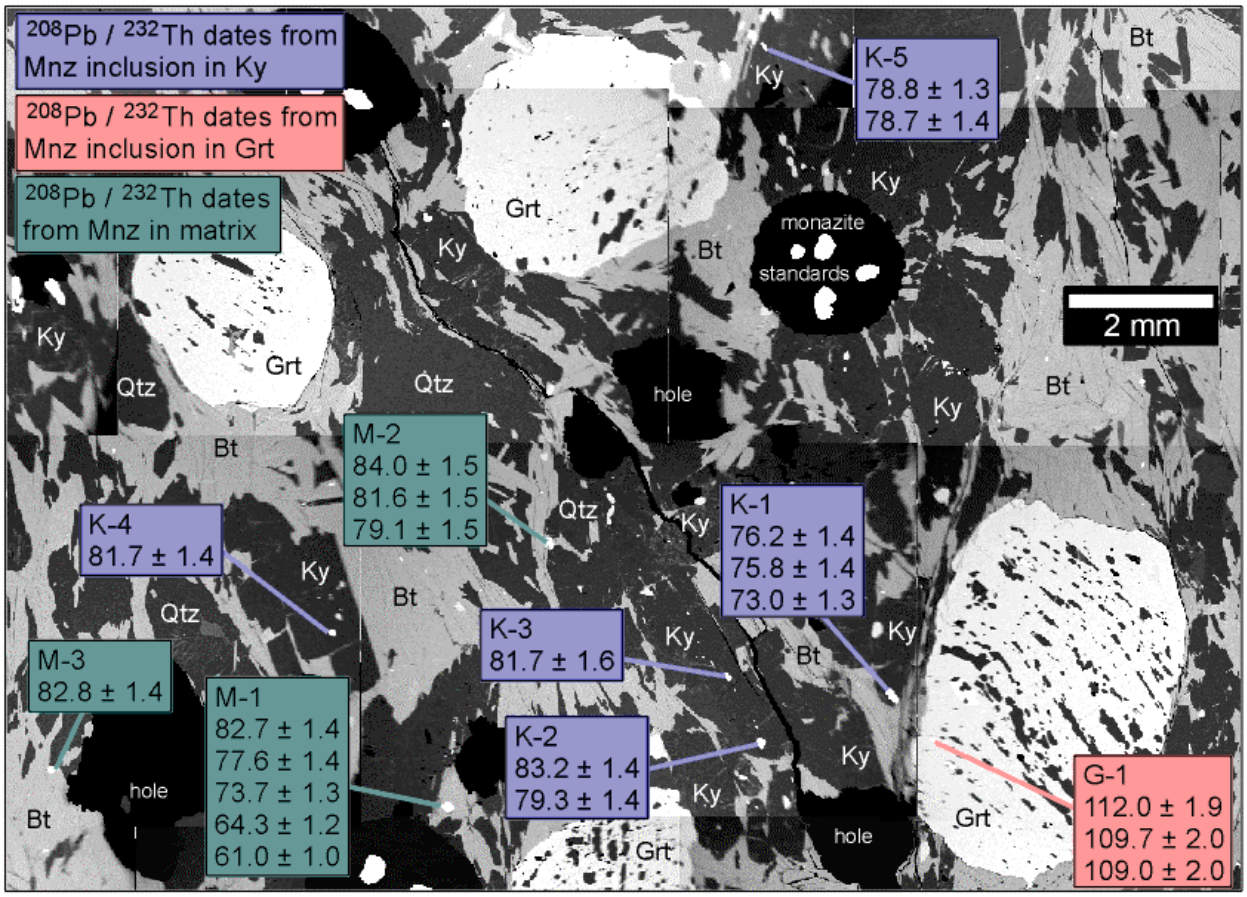

Figure 11. BSE image of a thin section from sample 1 showing the location of monazites dated with the SHRIMP and the $^{208}Pb/^{232}Th$ ages (1σ uncertainty). Mineral abbreviations after Kretz (1983).

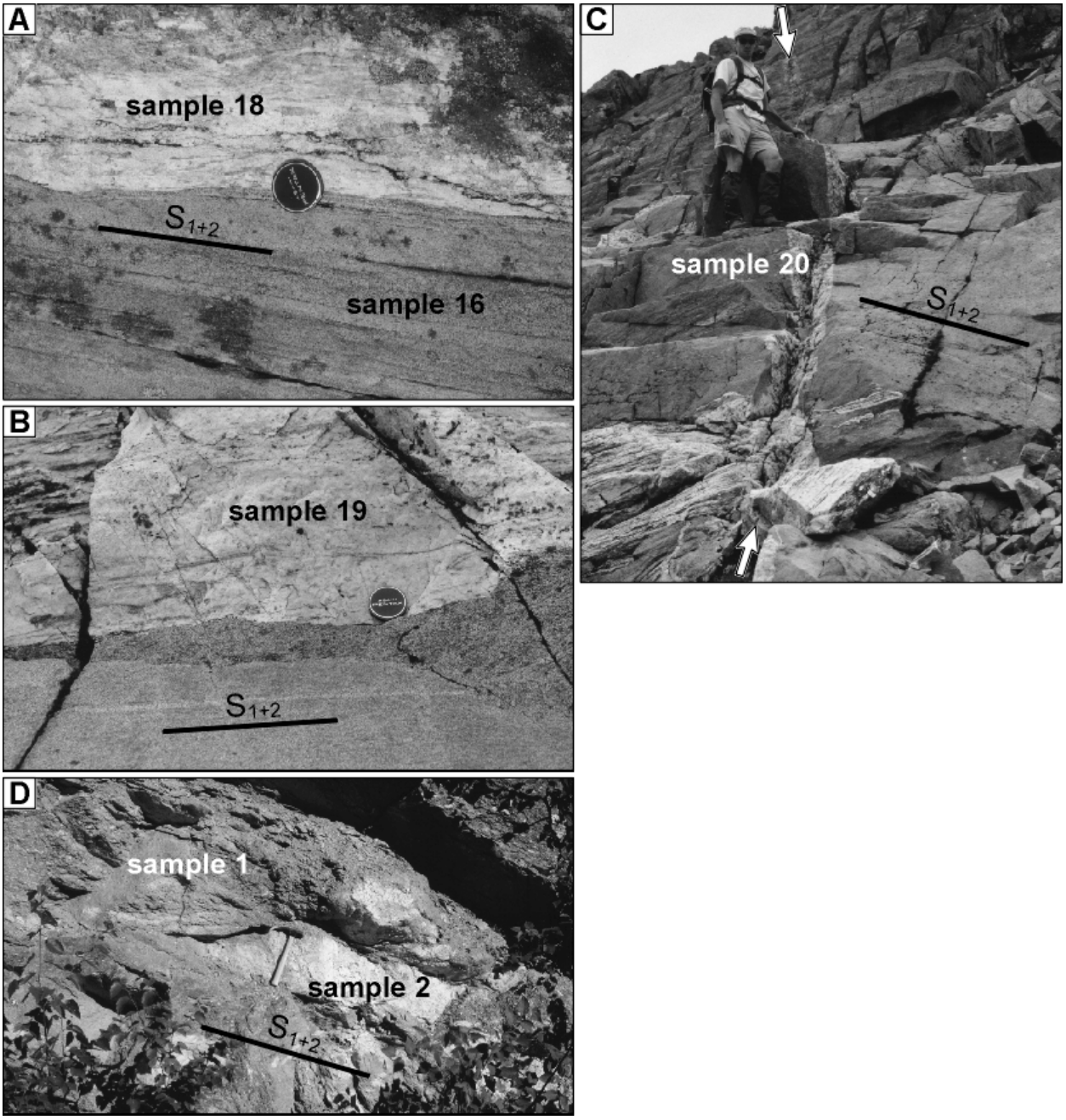

Figure 12. Dated granitoid rocks. (a) sample 18 (interpreted as 147 ± 11 Ma) is from a pegmatite layer that is concordant with S_{1+2} in the host semipelitic schist (sample 16) and contains a strong layer-parallel foliation. (b) sample 19 (171 ± 12 Ma) is from a pegmatite layer that is concordant with S_{1+2} in the host psammite and contains a strong layer-parallel foliation. (c) sample 20 (72.0 ± 0.5 Ma) is from a vertical pegmatite dyke (between arrows) that is highly discordant to S_{1+2} in the host psammite and lacks planar and linear deformation fabrics. View is to the south. (d) sample 2 (60.7 ± 0.5 Ma) is from a leucosome lens that is concordant with S_{1+2} in the host migmatitic kyanite schist (sample 1). It is one boudin in a train of leucosome boudins. View is to the east.

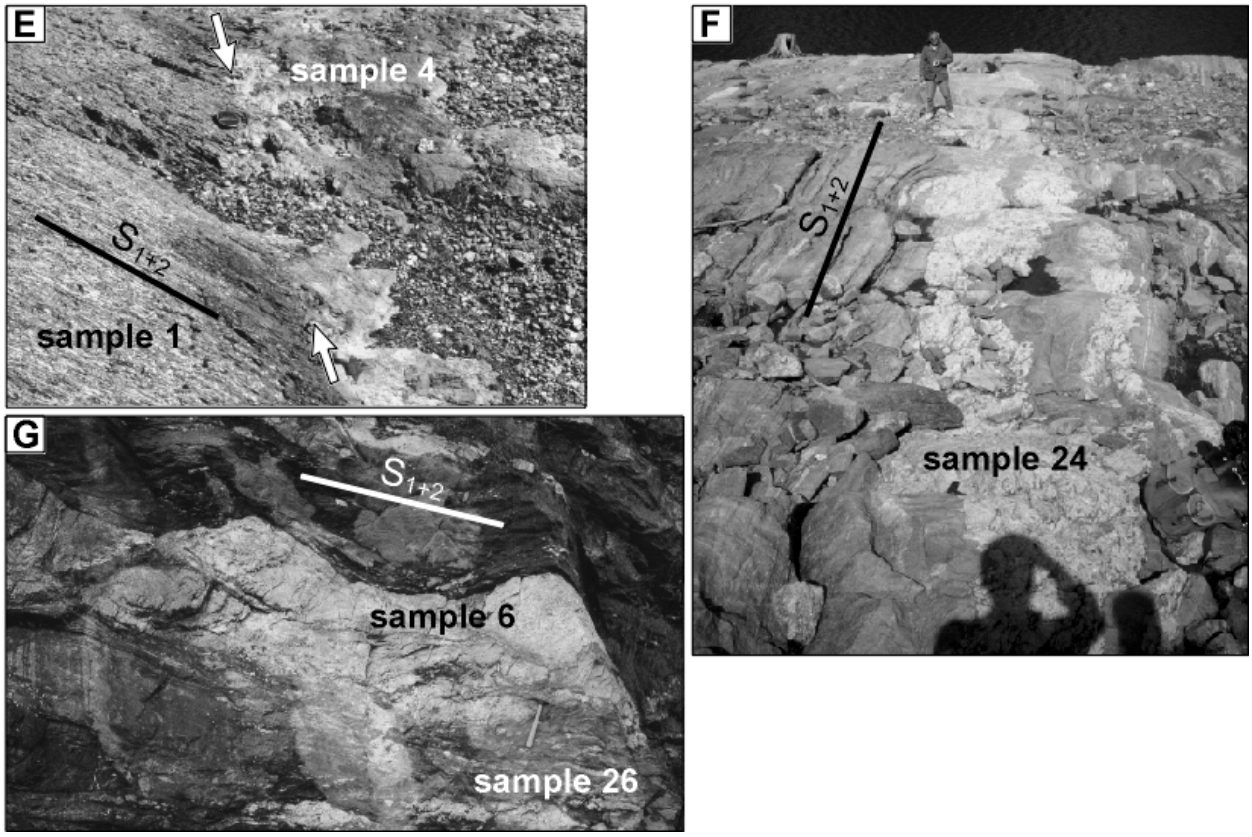

Figure 12 (*continued*). (e) sample 4 (58.4 ± 0.5 Ma) is from a vertical pegmatite dyke that is highly discordant to S_{1+2} in the host migmatitic kyanite schist (contact with schist lies between arrows). It lacks planar and linear deformation fabrics at the handspecimen scale. View is to the south. (f) sample 24 (63.5 ± 0.5 Ma) is from a pegmatite layer that is concordant with S_{1+2} in the host migmatitic kyanite schist and contains a layer-parallel foliation. The layer has been pulled apart into boudins and it appears to have intruded along S_{1+2}. View is to the northwest. (g) sample 6 (122.0 ± 1.0 Ma) is from a leucogranite layer that is concordant with S_{1+2} in the host migmatitic kyanite schist (sample 26) and contains a layer-parallel foliation. The layer has been pulled apart into boudins. View is to the east.

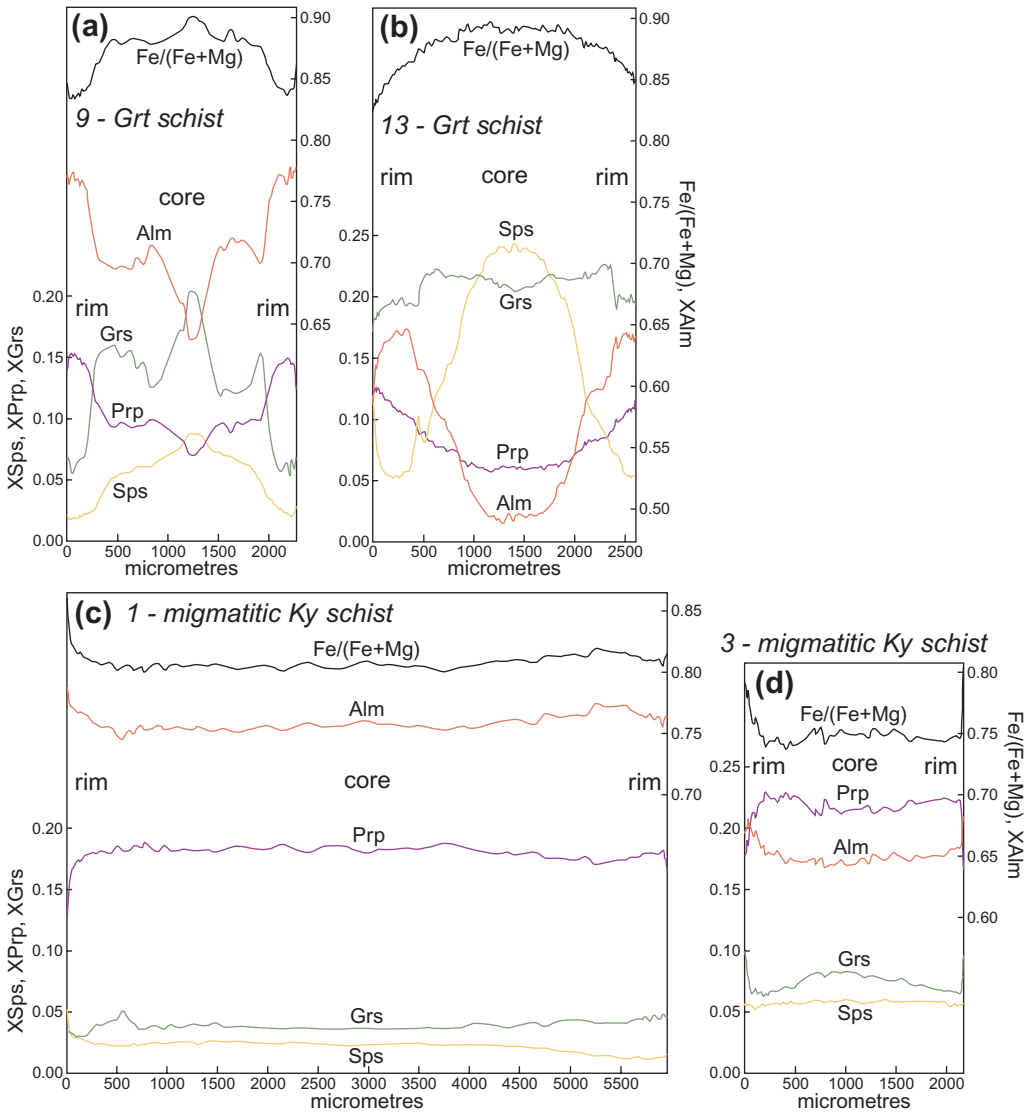

Figure 13. Profiles of garnet zoning in samples 1, 3, 9, 13 as determined with an electron microprobe. Mineral abbreviations after Kretz (1983).

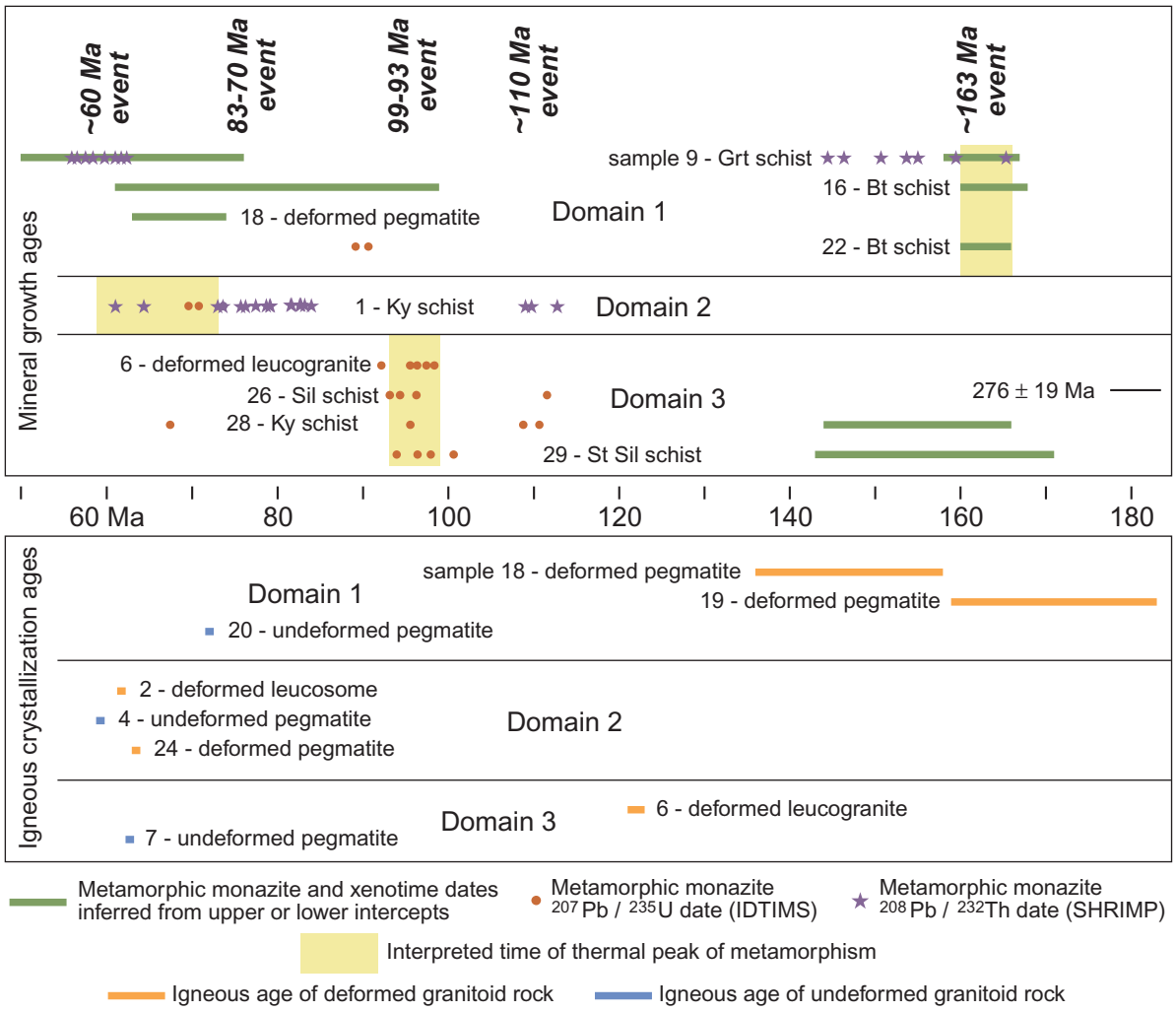

Figure 14. Timeline showing metamorphic mineral growth ages (top) and igneous crystallization ages (bottom) that are interpreted from the U-(Th)-Pb data. Samples are grouped by domain. Mineral abbreviations after Kretz (1983).